Modelling Heat And Mass Flow Through Packed Pebble Beds: A Heterogeneous Volume-Averaged Approach

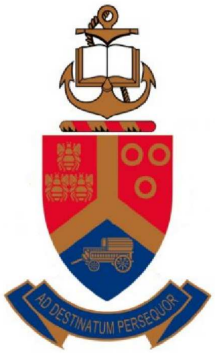

Coert Johannes Visser

Department of Mechanical and Aeronautical Engineering

University of Pretoria

Supervised by Prof. A.G. Malan and Prof. J.P. Meyer

A dissertation submitted in partial fulfilment of the requirements for the degree

Master of Engineering (Mechanical Engineering)

in the Faculty of Engineering, Built Environment and Information Technology

April 2007

Acknowledgements

I would like to thank my primary supervisor, Prof. Arnaud G. Malan. His guidance, hard work and infectious enthusiasm were essential to complete this work. I would also like to thank my co-supervisor, Prof. J. P. Meyer for his support. Recognition and thanks is also due to *North-West University* and *M-Tech Industrial* for the financial and technical support in undertaking the work presented here. Thank you in particular to Prof. C. G. du Toit and Mr. J. van der Merwe.

Abstract

This work details modelling buoyancy-driven viscous flow and heat transfer through heterogeneous saturated packed pebble beds via a set of volume-averaged conservation equations in which local thermal disequilibrium is accounted for. The latter refers to the two phases considered viz. solid and fluid, differing in temperature. This is effected by describing each phase with its own governing equation. Further to the aforementioned, the governing equation set is written in terms of intrinsic volume-averaged material properties that are fully variant with respect to temperature. The heterogeneous solid phase is described with a porosity field varying from 0.39 to 0.99. The intent of the stated upper bound is to explicitly model typical packed bed near-wall phenomena such as wall-channelling and pebble-wall heat transfer as true to reality as possible, while maintaining scientific rigour. The set of coupled non-linear partial differential equations is solved via a locally preconditioned artificial compressibility method, where spatial discretisation is effected with a compact finite volume edge-based discretisation method. The latter is done in the interest of accuracy. Stabilisation is effected via JST scalar-valued artificial dissipation. This is the first instance in which an artificial compressibility algorithm is applied to modelling heat and fluid flow through heterogeneous porous materials. As a result of the aforementioned, calculation of the acoustic velocities, stabilisation scaling factors and allowable time-step sizes were revised. The developed technology is demonstrated by application to the modelling of SANA test cases, i.e. natural convective flow inside a heated porous axisymmetric cavity. Predicted results are shown to be within 12% of experimental measurements in all cases, while having an average deviation of only 3%.

Contents

List of Figures vi
Nomenclature ix

1 Introduction **1**
1.1 Background 1
1.2 Thesis Outline 3
1.3 Publication List 4
1.3.1 Journal Papers 5
1.3.2 Conference Paper 5
1.4 Purpose of the Study 5

2 Problem Formulation and Governing Equations **6**
2.1 Introduction 6
2.2 Governing Equations 9
2.3 Constitutive Equations 13
2.3.1 Porosity Distribution 13
2.3.2 Solid Matrix Drag Coefficient 16
2.3.3 Fluid-solid Interface Heat Transfer Coefficient 18
2.3.4 Effective Solid Thermal Conductivity 19
2.4 Material Properties 24
2.5 Boundary Conditions 24
2.6 Conclusion 27

3 Solution Procedure **28**
3.1 Introduction 28
3.2 Artificial Compressibility 29

3.3 Spatial Discretisation 31
3.4 Stabilisation 34
3.4.1 Numerical Discretisation 35
3.4.1.1 First-order Accurate Stabilisation: Upwinding . . 36
3.4.1.2 Higher-order Accurate Stabilisation: Characteristic Based Method 36
3.4.1.3 Higher-order Accurate Stabilisation: Artificial Dissipation 37
3.4.1.4 Stabilisation Evaluation Results and Conclusion . 37
3.4.2 Artificial Dissipation 40
3.5 Temporal Discretisation 42
3.6 Conclusion 43

4 Numerical Tests and Validation **44**
4.1 Introduction 44
4.2 Porous Channel Flow 45
4.3 SANA Test Set-up 46
4.4 Conclusion 56

5 Conclusion and Recommendations **57**
5.1 Conclusion 57
5.2 Recommendations and Future Work 58

A Material Properties **60**
A.1 Introduction 60
A.2 Material Properties: Helium 60
A.3 Material Properties: Graphite 62

B Characteristic Based Stabilisation **65**
B.1 Introduction 65
B.2 Method Outline 65

C Numerical Validation **69**
C.1 Introduction 69
C.2 SANA 69

References 81

List of Figures

2.1 Schematic of the SANA test set-up with central heating element taken from [51]. 7
2.2 Measured (Benenati & Brosilow) radial void fraction distribution for packed beds of uniform spheres contained by a solid wall, as well as the exponential correlation of Hunt & Tien as used in this work. The distance from the solid wall is given in terms of sphere diameters (d_p). 14
2.3 Contour plot of the 2-D porosity distribution as applied to the SANA test case. 16
2.4 Typical porosity distribution (ε) and matrix drag in vertical direction (B_2) based on maximum vertical velocity. The graph is given for the porosity range under which $\mathbf{B}$ is valid, i.e. $\varepsilon < 0.8$. 18
2.5 Modified ZBS correlation (k_{eff}^{nw}) and effective thermal conductivity, based on the original model by Zehner & Schlünder [79] (k_{eff}^{H}), calculated at a section through the vertical centreline for the 5 kW (top left) and 35 kW (bottom left) SANA test cases. The final values of k_{eff} employed in this work for the respective test cases are shown on the right-hand side. 23
2.6 Schematic diagram of the variables involved in calculating the heat flux Neumann boundary condition. In the figure, $\langle T_s \rangle^s|_w$ and $\langle T_s \rangle^w$ denote the pebble temperature at the wall and actual wall temperature respectively. 25

3.1 Schematic diagram of the construction of the median dual-mesh on a stretched grid. The volume-averaged centroid position of volume $\mathcal{V}_m$ is indicated by $\boldsymbol{x}^*_{\mathcal{V}_m}$, and Υ_{mn} depicts the edge connecting nodes m and n. 32
3.2 Predicted solution to the advection-diffusion equation compared to the analytical solution for a Peclet number of 2. Predictions as obtained on an equal-spaced (left) and preferentially stretched (right) mesh containing five elements are shown. CB and JST denote the *characteristic based* and *artificial dissipation* stabilisation schemes respectively. The subscripts L and R indicate the left and right boundaries respectively. 38
3.3 Predicted solution to the advection-diffusion equation compared to the analytical solution for a Peclet number of 10. Predictions as obtained on an equal-spaced (left) and preferentially stretched (right) mesh containing five elements are shown. 39
3.4 Predicted solution to the advection-diffusion equation compared to the analytical solution for a Peclet number of 50. Predictions as obtained on an equal-spaced (left) and preferentially stretched (right) mesh are shown. 39

4.1 Porous channel mesh. 45
4.2 Channel porosity distribution. 45
4.3 Porous channel velocity (left) and static pressure (right) distribution. 46
4.4 Schematic diagram of the SANA test set-up (left) with central heating element taken from [51] and the representative axisymmetric mesh used (right). 47
4.5 Schematic diagram of the geometry and boundary conditions applied. Here, r_i and r_o denote the internal and external radii respectively and q_{input} and q_{solid} the respective heat fluxes as calculated using Equations (2.28) and (2.31). 48
4.6 Porosity distribution at the horizontal (left) and vertical (right) centrelines, as applied to the variable porosity SANA test cases. . 49

4.7 Vertical velocities in radial section at 0.5 m vertical elevation for constant and variable porosity 5 kW test cases. 49
4.8 Vertical velocities in radial section at 0.5 m vertical elevation for constant and variable porosity 35 kW test cases. 50
4.9 Predicted temperature distribution of the solid (s) and fluid (f) phases at the inner wall for the variable porosity 5 kW (left) and 35 kW (right) test cases. 50
4.10 Streamlines for the variable porosity 5 kW (left) and 35 kW (right) cases. 51
4.11 Predicted pebble temperature distribution compared to experimental (exp.) measurements for the 5 kW (left) and 35 kW (right) cases. The comparisons are done at three different heights. The top figures detail the constant porosity test cases, and the bottom figures the variable porosity test cases. 53
4.12 Normalised temperature disparity between predicted and measured solid-phase temperatures for the 5 kW (left) and 35 kW (right) cases. The top figures detail the constant porosity test cases, and the bottom figures the variable porosity test cases. 54
4.13 Average residual for the constant porosity 5 kW (left) and 35 kW (right) cases. 55
4.14 Average residual for the variable porosity 5 kW (left) and 35 kW (right) cases. 55

C.1 Predicted pebble temperature distribution at 0.09 m vertical elevation compared to experimental measurements for 5 kW (left) and 35 kW (right). 70
C.2 Predicted pebble temperature distribution at 0.5 m vertical elevation compared to experimental measurements for 5 kW (top) and 35 kW (bottom). 71
C.3 Predicted pebble temperature distribution at 0.91 m vertical elevation compared to experimental measurements for 5 kW (top) and 35 kW (bottom). 72

Nomenclature

Roman Symbols

a_T	Generalised artificial compressibility preconditioning coefficient: fluid-phase energy equation
a_u	Generalised artificial compressibility preconditioning coefficient: continuity and momentum equations
$\mathcal{A}$	Surface $[m^2]$
$\mathcal{A}_{mn}$	Control volume bounding surface associated with the edge connecting nodes m and n $[m^2]$
$\boldsymbol{B}$	Solid-phase matrix drag vector $[kg/m^2\ s^2]$
c_τ	Pseudo-acoustic velocity $[m/s]$
$\boldsymbol{C}_{mn}$	Internal edge coefficient of the edge connecting nodes m and n $[m^2]$
C_p	Specific heat at constant pressure $[J/kg\ K]$
d_p	Particle/sphere diameter $[m]$
D	Reactor tube diameter $[m]$
$\boldsymbol{D}$	Artificial dissipation vector for application to the Navier-Stokes equation set
$\mathcal{D}$	Stabilisation component
E_s	Solid phase Young's modulus $[N/m^2]$

f	Form factor accounting for heat transfer effects due to pebble deformation (Related to calculation of k_{eff}) $[N]$
$\boldsymbol{F}$	Volume-averaged governing equation set convective flux matrix
$\boldsymbol{g}$	Gravitational acceleration vector ($\mid \boldsymbol{g} \mid \approx 9.81$) $[m/s^2]$
$\boldsymbol{G}$	Volume-averaged governing equation set viscous flux matrix
h_{fs}	Superficially averaged fluid-solid interface heat transfer coefficient $[W/m^2\ K]$
h_r	Wall-bed interface radiative heat transfer coefficient $[W/m^2\ K^4]$
h_w	Interfacial conductance (contact resistance) $[W/m^2\ K]$
$\boldsymbol{H}$	Volume-averaged governing equation set pressure derivative vector
$\mathfrak{I}$	Temporal domain $[s]$
k	Thermal conductivity $[W/m\ K]$
k_{eff}	Superficially averaged bed effective thermal conductivity $[W/m\ K]$
$\mathfrak{L}$	One-dimensional domain bound $[m]$
l_{mn}	Length of the discrete edge connecting nodes m and n $[m]$
$\boldsymbol{n}$	Outward-pointing unit vector perpendicular to a domain boundary
N_A	Number of particles per unit area (Related to calculation of k_{eff}) $[m^{-2}]$
N_L	Number of particles per unit length (Related to calculation of k_{eff}) $[m^{-1}]$
p	Fluid-phase static pressure $[Pa]$
p_s	Pressure due to weight of particles in pebble bed $[Pa]$
$\boldsymbol{Q}$	Incompressible volume-averaged governing equation set primitive variable vector
r	Radius $[m]$

R_C	Convective component of RHS
R_D	Diffusive component of RHS
$\boldsymbol{S}$	Volume-averaged governing equation set source vector
S	Structural parameter related to the volumetric arrangement of pebbles (Related to calculation of k_{eff})
S_F	Structural parameter related to the volumetric arrangement of pebbles (Related to calculation of k_{eff})
t	Time $[s]$
t_C	Maximum allowable time-step size based on the convective velocity of information propagation $[s]$
$\boldsymbol{t}_{mn}$	Unit vector parallel to the edge connecting nodes m and n
t_τ	Pseudo-time $[s]$
T	Temperature $[K]$
$\mathbf{u}$	Fluid-phase velocity vector $[m/s]$
$\mathcal{V}$	Volume $[m^3]$
$\boldsymbol{W}$	Compressible volume-averaged governing equation set primitive variable vector
$\boldsymbol{x}$	Spatial position (Vector from origin of coordinate axis) $[m]$

Greek Symbols

α	Arbitrary constant scalar variable
β	Deformation factor (Related to calculation of k_{eff})
$\Delta\chi$	Effective element size employed for maximum time-step size calculations $[m]$

ϵ	Solid-phase Poisson's ratio
ε	Porosity or void fraction
$\varepsilon_{c_{\tau conv}}$	Variable related to the calculation of $c_{\tau conv}$
ε_4	Empirical constant related to the calculation of the artificial dissipation vector $\boldsymbol{D}$
θ	Cylindrical coordinate direction
ϑ	Scalar field (function of $\boldsymbol{x}$)
κ	Conductivity ratio ($\langle k_s \rangle^s / \langle k_f \rangle^f$)
λ	Maximum eigenvalue associated with a specific equation type $[m/s]$
Λ	Artificial dissipation scaling coefficient vector $[m^3/s]$
μ	Fluid-phase coefficient of viscosity $[kg/m\ s]$
ξ	Thermal radiative emissivity
ϖ_R	Radiative component of near-wall effective thermal conductivity (Related to calculation of k_{eff})
ρ	Density $[kg/m^3]$
σ	Stefan-Boltzmann constant ($\sigma \simeq 5.67 \times 10^{-8}$) $[W/m^2\ K^4]$
σ_{vn}	Von Neumann number
$\boldsymbol{\tau}$	Fluid-phase viscous stress tensor $[kg/m\ s^2]$
Υ_{mn}	Discrete edge connecting nodes m and n
ϕ	Arbitrary scalar variable
Φ	Constant boundary value of ϕ
Ψ	Variable forming part of *Damköhler's* equivalent thermal conductivity (Related to calculation of k_{eff})

Superscripts

ad	Artificial dissipation
$*$	Property evaluated at the centroid of a discrete element/volume
f	Fluid phase
H	Homogeneous
k	General tensor notation spatial index
nw	Near wall
s	Solid phase
sc	Solid-phase and interface contact conduction component of k_{eff}
sf	Solid-fluid phase conduction component of k_{eff}
sr	Solid-phase conduction and radiative component of k_{eff}
w	Porous bed bounding wall

Subscripts

b	Homogeneous bed property on the edge of the near-wall region
$cont$	Continuity/Related to mass transfer
$conv$	Convective
d_p	Based on particle diameter
$diff$	Diffusive component
$enerf$	Related to fluid-phase energy
$eners$	Related to solid-phase energy
f	Fluid phase
$\overline{f}$	Edge-averaged quantity

$\overline{g}$	Finite volume-averaged quantity
ζ	General tensor notation index
H	Homogeneous
i	Inner
j	General tensor notation spatial index
k	General tensor notation spatial index
L	Domain boundary left
m	Discrete node number
max	Maximum
min	Minimum
mom	Related to momentum transfer
n	Discrete node number
$norm$	Normal/perpendicular
nw	Near wall
o	Outer
p	Elementary particle making up porous bed, viz. pebble
R	Domain boundary right
s	Solid phase
$tang$	Tangential component
$\mathcal{V}$	Property associated with volume $\mathcal{V}$
w	Porous bed bounding wall
ψ	Arbitrary phase

∞	Reference condition

Mathematical Operators

$D\bullet$	Lagrangian derivative of $\bullet$
$\Delta\bullet$	Increment in $\bullet$
δ	Kronecker's delta
$\langle\bullet\rangle^{\psi}$	Intrinsic volume average of $\bullet$ of phase ψ
$\mid\bullet\mid$	Norm/magnitude of vector quantity $\bullet$
$\partial\bullet$	Partial derivative of $\bullet$

Non-dimensional Numbers

Nu_{d_p}	Nusselt number $\left(\frac{h_{fs}d_p}{\langle k_f\rangle^f}\right)$
Pe	Peclet number $\left(\frac{u_1\mathcal{L}}{\alpha}\right)$
Pr	Prandtl number $\left(\frac{\langle C_{p_f}\rangle^f\langle\mu_f\rangle^f}{\langle k_f\rangle^f}\right)$
Re_{d_p}	Reynolds number $\left(\frac{\langle\rho_f\rangle^f\varepsilon\mid\langle\boldsymbol{u}\rangle^f\mid d_p}{\langle\mu_f\rangle^f}\right)$

Acronyms

AC	Artificial Compressibility
CB	Characteristic Based
CFD	Computational Fluid Dynamics
ECS	Energy Conversion System
$HTGR$	High-temperature Gas-cooled Reactors
$IAEA$	International Atomic Energy Agency
JST	Jameson-Schmidt-Turkel scalar valued dissipation

KTA	Nuclear Safety Standards Commission
LTE	Local Thermal Equilibrium
RHS	Right-hand side
$TRISO$	Tristructural-isotropic
ZBS	Zehner-Bauer-Schlünder model for effective thermal conductivity (k_{eff})

Notes on Notation

In this work, both vector and index notations are used. Vectors and matrices are printed in **bold**. Einstein's summation convention is implied in the case of index notation.

Chapter 1

Introduction

1.1 Background

Development of so-called fourth-generation inherently safe nuclear power reactors is currently supported by several countries, including South Africa [62]. Several factors played a role in the renewed interest in nuclear power developments, the more important of these arguably being the ever-increasing worldwide demand for energy [22, 61], environmental impact concerns over conventionally fired power stations [12, 22, 61, 62], and an unstable oil market [9, 12]. South Africa currently heads the development of a commercially viable fourth-generation reactor, namely the pebble-bed modular reactor (PBMR). This nuclear, high-temperature gas-cooled reactor (HTGR) is described by some as inherently safe, and promises to generate less nuclear waste and be less expensive than light water reactors currently in use [62]. South Africa expects to complete construction of a demonstration plant near the city of Cape Town by 2011 [54].

Alongside the commercial interest in HTGRs, renewed interest into the technical aspects of such developments followed naturally, as these nuclear devices involve fairly complex technology [61]. Considering, for example, high-temperature reactors which utilise a packed pebble bed, specific requirements need to be adhered to in order to ensure safe operation. One such example is the PBMR, where maintaining a maximum fuel temperature below 1 600 $^{\circ}C$ is essential to ensure the

integrity of the TRISO[1]-coated particles [37]. Analysis and simulation capabilities are therefore crucial to not only aid the design of HTGRs, but also help ensure their safe operation through various validation and verification exercises [30]. Considering the thermodynamic analysis of a typical high-temperature reactor and its energy conversion system (ECS), numerical techniques [6, 15, 72] recently showed promise to provide detailed information as to the complex mechanisms of flow, heat and mass transfer prevailing, although significantly lagging experimental development of HTGRs, that already started in the 1950′s [32, 42, 72].

Computational fluid dynamics (CFD) is today known to allow the quantitative prediction of operating conditions of complete systems, thereby reducing time and experimental effort. Furthermore, CFD allows solutions to mathematical relations unobtainable analytically. The latter implies that predictions of complex flow and heat transfer phenomena can now be made, thereby allowing for the prediction of parameters and trends where physical measurements are not necessarily possible, as is typically the case with nuclear reactors. CFD can thus be a valuable tool in a designer's arsenal if used responsibly, knowing the many limitations and assumptions associated with it. Continual advances in both computing power and numerical solution techniques, however, allow scientists to incrementally improve mathematical modelling capabilities. This is essential to meet the growing need for the accurate quantitative description of the involved physics in as detailed a manner as possible. Note that simulating flow and heat transfer through porous media is not limited to reactor cores. It finds application in, among others, chemical reactors [8] and electronic cooling analysis, where the increase in heat-generated density [77, 78] poses a threat to the life, operation [18] and further development [82] of the devices.

The work undertaken in this study is aimed at serving a number of purposes. The first is the investigation into the thermodynamic modelling of a packed pebble bed, and the respective building blocks that it consists of, i.e. governing equations, boundary conditions and a suitable numerical solution procedure. Regarding the latter, this work endeavours to further the development of numerical techniques and numerical modelling technology for the quantitative simulation of flow and heat transfer through packed pebble beds. Lastly, the work documented

[1]Tristructural-isotropic

forms part of a collective effort within the research group to produce numerical results for the SANA [51] benchmark test case. This was done as part of an independent verification and validation exercise in partnership with *North-West University* in order to validate the *Flownex* commercial systems CFD code developed by *M-Tech Industrial*.

1.2 Thesis Outline

The overall objective of this study, preempted by the above, is to numerically model steady two-dimensional axisymmetric natural convective flow and heat transfer through packed pebble beds. Specifically, flows through randomly packed pebble beds were considered, with the distinct objective of making as little assumptions as possible, and thus presenting a rigorous application of the mathematical literature specific to this field. The significance of considering natural convective flow is due to the SANA test set-up, while being of relevance to a loss-of-active-cooling-accident [72] in real nuclear reactors. Such an incident requires the heat inside the reactor vessel to be transported by passive means to the extent of maintaining critical temperature margins. A volume-averaged continuum modelling approach is followed where two phases are considered, viz. a solid phase representing the pebbles and a fluid phase representing the coolant circulating through the solid matrix. Conservation of mass, momentum (Navier-Stokes) and energy is applied to the fluid phase, while conservation of energy is enforced on the solid phase. The set of governing equations is written in terms of intrinsic volume-averaged[1] quantities that are temperature dependent. The multiple energy equations effectively allow solving for two unique temperatures for the respective phases (thermal disequilibrium). The governing equations employ constitutive equations to represent the microscopic behaviour present in fluid flow and heat transfer through the porous matrix, compensating for the resolution lost through the process of volume-averaging. Chapter 2 details the problem formulation consisting of the governing equation set, constitutive equations and boundary conditions employed.

[1]The method of volume-averaging is typically employed to reduce porous materials such as pebble beds to a continuum in computational space.

The set of governing equations, analytically valid in a point, is to be rewritten in discrete algebraic form through application of both a spatial and temporal discretisation strategy. This renders a set of numerically resolvable equations. A vertex-centred finite volume technique is used in this work for spatial discretisation, while an explicit single-stage time-marching method is used for temporal discretisation. The material properties are considered variant with respect to temperature, but invariant with respect to change in pressure. The consequence of the latter is a so-called numerically stiff system, addressed in this work through the method of *artificial compressibility*. The central-difference explicit nature of the numerical scheme employed, deems it unconditionally unstable, therefore, requiring an artificial method to resolve odd-even decoupling. Two potential stabilisation schemes are reviewed, viz. *artificial dissipation* and a *characteristic based* method. The focus of Chapter 3, is therefore, the solution procedure where the following are considered: the spatial and temporal discretisation strategy, artificial compressibility and the stabilisation scheme employed.

Verification of the developed numerical technology is detailed in Chapter 4. Two types of test cases are considered. Firstly, a uniform two-dimensional channel with a one-dimensional sharply varying porosity distribution wherein inviscid isothermal flow is modelled. This is to evaluate the stability of the numerical scheme at resolving flow fields with large gradients in porosity, i.e. strongly heterogeneous. To evaluate the full spectrum of current numerical capability for solving flow and heat transfer through randomly packed pebble beds, the SANA benchmark test case, as detailed by the *IAEA* [33], is modelled. Both constant and variable porosity distributions are considered when modelling the SANA test case, and the results compared against experimental measurements.

Chapter 5 concludes the findings and results from this work. Additionally, current shortcomings are highlighted and recommendations for future work made.

1.3 Publication List

This work resulted in the following publications:

1.3.1 Journal Papers

- C. J. Visser, A. G. Malan and J. P. Meyer. Modelling of buoyancy-driven flow in saturated porous materials via an artificial compressibility method. *Numerical Heat Transfer, Part B*, 2007. **Submitted for review**.

- C. J. Visser, A. G. Malan and J. P. Meyer. An artificial compressibility algorithm for modelling natural convection in heterogeneous saturated porous media. *International Journal for Numerical Methods in Engineering*, 2007. **Submitted for review**.

1.3.2 Conference Paper

- A. G. Malan, C. J. Visser and J. P. Meyer. Modelling heat and fluid flow through packed beds - a density-based vertex-centred methodology. In *HTR2006: 3rd International Topical Meeting on High-Temperature Reactor Technology*, Johannesburg, South Africa, 2006.

1.4 Purpose of the Study

In summary, the purpose of this study is to develop numerical modelling capability able to extensively simulate flow and heat transfer through heterogeneous porous media, with specific application to randomly packed pebble beds. An artificial compressibility approach is used and spatial discretisation affected via a vertex-centred finite volume method. Artificial dissipation is employed for stabilisation purposes.

Chapter 2

Problem Formulation and Governing Equations

2.1 Introduction

This chapter details the mathematical formulation of the problem at hand, viz. flow and heat transfer through randomly packed pebble beds, the solution of which will be sought through numerical means. The equations are formulated so as to present a generic set of conservation laws, while the constitutive equations are specific to beds of stationary packed spherical particles. A typical reactor pebble bed consists of an annular vessel filled with equal-sized pebbles, similar to that shown in Figure 2.1. The pebbles (solid phase) are randomly packed and the working fluid (fluid phase) circulates through the interstitial voids between the pebbles, be it through forced or natural convection.

To date, several modelling approaches exist to predict the flow and heat transfer phenomena prevailing in packed pebble beds. The two significant approaches are arguably pore-scale modelling or a continuum approach, referred to as a *generalised* model. Pore-scale modelling [44, 50, 53] explicitly resolves flow features in detail, which includes actual flow patterns in bed interstitial voids. The resolution of the continuum type approach is limited to the size of the representative elementary volume and the availability of reliable constitutive equations (typically based on experimental data). Applying pore-scale modelling to realistic engineering problems such as randomly packed pebble-bed nuclear reactors is, however,

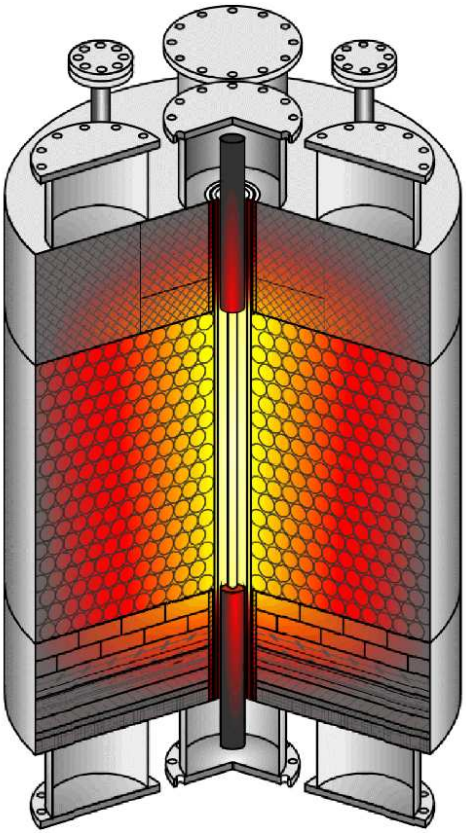

Figure 2.1: Schematic of the SANA test set-up with central heating element taken from [51].

computationally still prohibitively expensive (Morris *et al.* [50]). For this reason, the continuum or generalised methodology was employed in this work.

The *generalised* or continuum model was initiated by Whitaker [75], and is based on his method of volume-averaging. This approach attempts to find an acceptable compromise between the two opposing ideals of solution accuracy and computational cost. The method employs governing equations written in terms of intrinsic volume-averaged quantities, while the constitutive relations in the governing equations account for pore-scale phenomena in a volume-averaged sense. The ability of the generalised model to resolve flow and heat transfer through porous media is illustrated by various authors. Firstly, Nithiarasu *et al.* [52] modelled buoyancy-driven flow in fluid-saturated non-Darcian porous media, indicat-

ing that the model reduces to the Navier-Stokes equations for a porosity[1] equal to one and that it agrees with the generalised model as used by Vafai *et al.* [69]. The aforementioned authors, similar to others [41, 56], employed what is known as a *pseudo-homogeneous* or *local thermal equilibrium*[2] (LTE) model, where a single-energy equation is used. This method is, in consequence, only valid when a negligible temperature difference exists between the phases. Another example from the literature is application to gas-fluidised beds by Kuipers *et al.* [40], where a continuum description is used to model the two fluids in suspension.

Further, the abovementioned generalised type model has been applied with reasonable success to describe flow and heat transfer in packed-bed nuclear reactors [6, 15, 71, 72], where various levels of complexity have been introduced. Becker & Laurien [6], for example, pointed out that the assumption of *local thermal equilibrium* between the solid phase and working fluid is inadequate, necessitating multiple equations to enforce conservation of energy for the respective phases (also referred to as a *pseudo-heterogeneous*[3] model). This technique is also supported by, among others, du Toit *et al.* [15], Gidaspow [24], Gunn [29] and Kuipers *et al.* [40]. In addition to solving for two energy equations for the solid and fluid phases respectively, du Toit *et al.* [15] introduced an additional energy equation, enforcing energy conservation for a representative pebble, therefore resolving the radial temperature distribution in a representative pebble. This additional complexity is, however, of importance when internal heat generation inside the pebbles (due to nuclear reactivity) as well as transient characteristics is dominant. It was therefore not considered in this work.

The sections to follow detail the governing equations and accompanying assumptions (Section 2.2), constitutive equations and their validity (Section 2.3), material properties used (Section 2.4) and the boundary conditions employed (Section 2.5).

[1] Porosity is defined as the ratio of the void fraction volume to the total volume.

[2] *Local thermal equilibrium* implies negligible temperature *difference* between phases at a *specific point in space*.

[3] *Pseudo-heterogeneous* refers to a model where a distinction is made between the temperature of the respective phases modelled, e.g. a fluid and solid phase. Here, separate energy equations are solved in the case of a packed bed where the pebbles are stationary.

2.2 Governing Equations

The generalised set of governing equations employed in this work is similar to that used by, among others, Becker & Laurien [6] and Vafai [68]. The similarity lies in the sense that the volume-averaging technique, coupled with semi-empirical formulae, is used to describe natural convective flow through a saturated rigid porous material. As mentioned previously, in this work, the latter is specific to randomly packed pebble beds. Similar to others [6, 15, 40], a two-phase system (fluid and solid phase) is considered and the following assumptions made:

- Viscous dissipation effects as well as the kinetic energy contribution to the fluid-phase total energy are assumed negligible. This is due to the velocities considered being significantly below sonic velocities.

- Further to the previous assumption, fluid-phase material properties are assumed to be invariant with respect to variation in the pressure field (a condition generally known as incompressible flow). Fluid pressure incompressibility is a result of both small speeds as well as natural convection flows not resulting in large pressure gradients across the bed. Fluid-phase material properties, with the exception of specific heat are, however, to be fully variant with respect to temperature.

- Solid-phase material properties are assumed to be invariant with respect to both temperature and pressure with the exclusion of thermal conductivity. The latter is taken as variant with respect to temperature.

- The solid matrix is rigid and solid particles impermeable.

- No chemical reactions or phase change occurs.

- In the continuum computational domain, the solid porous phase is assumed isotropic and heterogeneous, i.e. invariant with respect to coordinate rotation but variant with respect to coordinate translation. The spatially varying porous structure is represented with the scalar field quantity of porosity. A porosity field variation of 0.39 to 0.99 is allowed for in this work. The intent of the stated upper bound is to explicitly model typical

packed-bed near-wall phenomena, such as wall channelling and pebble-wall heat transfer, as true to reality as possible.

- Heat transfer via thermal dispersion is assumed to be negligible.

In addition to the above, it is assumed that there is no significant temperature gradient within a specific pebble (as noted previously). This is motivated by the fact that steady buoyancy-driven flows will be modelled. The governing equations are in general written in terms of intrinsic volume-averaged quantities. The aforementioned is defined for a scalar field $\vartheta_\psi\left(t, \mathbf{x} \in \mathcal{V}_\psi\right)$ of arbitrary phase ψ at time t and spatial position $\mathbf{x}$ as:

$$\langle \vartheta_\psi \rangle^\psi = \langle \vartheta_\psi \rangle^\psi \left(t, \mathbf{x}_\mathcal{V}\right) = \frac{1}{\mathcal{V}_\psi} \int_{\mathcal{V}_\psi(\mathbf{x})} \vartheta_\psi \left(t, \mathbf{x}\right) d\mathcal{V} \tag{2.1}$$

where $\mathcal{V}_\psi\left(\mathbf{x}\right)$ is the volume of phase ψ over which averaging is applied with geometric centre $\mathbf{x}_\mathcal{V}$. Distinction between a fluid and solid phase is made in this work, therefore ψ will be replaced by f or s respectively.

The governing system of equations to be presented differs from those employed by others [6, 15, 40] in that a clear distinction is made between superficial and intrinsic averaged quantities. Furthermore, the equations are presented in a generic, two-dimensional rectangular/axisymmetric format, where the standard two-dimensional Navier-Stokes equation set for a Cartesian coordinate system is recovered by setting the porosity (ε) and radius (r) equal to one (the porosity is defined below). The governing system of equations now follows.

Mass conservation of the fluid phase reads:

$$\frac{\partial \left(\varepsilon r \langle \rho_f \rangle^f\right)}{\partial t} + \frac{\partial}{\partial x_j}(\varepsilon r \langle \rho_f \rangle^f \langle u_j \rangle^f) = 0 \tag{2.2}$$

where $\langle \rho_f \rangle^f$ is the intrinsic volume-averaged density of the fluid phase, $\langle u_j \rangle^f$ is the intrinsic velocity component of the fluid phase in Cartesian coordinate direction x_j, and r is the axisymmetric radius. The latter is invariant in the pore-scale (microscopic) domain and therefore variant only at volume-averaged (macroscopic) level. The porosity or void fraction is denoted by ε and calculated as:

$$\varepsilon = \varepsilon(\mathbf{x}_{\mathcal{V}}) = \frac{1}{\mathcal{V}} \int_{\mathcal{V}_f(\mathbf{x})} d\mathcal{V} \tag{2.3}$$

where $\mathcal{V}$ is the volume over which volume-averaging is applied, and contains both fluid- and solid phases.

Momentum conservation of the fluid phase reads:

$$\begin{aligned} &\frac{\partial(\varepsilon r \langle \rho_f \rangle^f \langle u_k \rangle^f)}{\partial t} + \frac{\partial}{\partial x_j}(\varepsilon r \langle \rho_f \rangle^f \langle u_j \rangle^f \langle u_k \rangle^f) + \varepsilon r \frac{\partial \langle p \rangle^f}{\partial x_k} \quad - \\ &\frac{\partial}{\partial x_j}(\varepsilon r \langle \tau_{kj} \rangle^f) - \varepsilon r \langle \rho_f \rangle^f \langle g_k \rangle^f - r B_k + \delta_{1k}(1 - \delta_{k\zeta}) \varepsilon \langle \tau_{33} \rangle^f \quad = \quad 0 \end{aligned} \tag{2.4}$$

where $\langle p \rangle^f$ denotes the intrinsically averaged fluid-phase static pressure, $\langle \tau_{kj} \rangle^f$ is the viscous stress term, $\langle g_k \rangle^f$ is the gravitational acceleration in direction x_k and B_k is the drag due to the solid matrix. The additional fluid-phase viscous stress term $\langle \tau_{33} \rangle^f$ is a result of the axisymmetric formulation used in this work, where the subscript 33 indicates a tensor component in the circumferential or θ coordinate direction, and δ_{kj} is Kronecker's delta. Note that for a two-dimensional cylindrical coordinate system, the radial direction r is assigned to the x_1 rectangular coordinate direction and $\zeta = 0$. Furthermore, application of the governing equation set to a rectangular coordinate system requires r and ζ to be set equal to one. The respective viscous stress components are given by:

$$\langle \tau_{11} \rangle^f = -\frac{2}{3} \langle \mu_f \rangle^f \left(\frac{1}{r} \frac{\partial}{\partial x_1} \left(r \langle u_1 \rangle^f \right) + \frac{\partial \langle u_2 \rangle^f}{\partial x_2} \right) + 2 \langle \mu_f \rangle^f \frac{\partial \langle u_1 \rangle^f}{\partial x_1} \tag{2.5}$$

$$\langle \tau_{12} \rangle^f = \langle \tau_{21} \rangle^f = \langle \mu_f \rangle^f \left(\frac{\partial \langle u_2 \rangle^f}{\partial x_1} + \frac{\partial \langle u_1 \rangle^f}{\partial x_2} \right) \tag{2.6}$$

$$\langle \tau_{22} \rangle^f = -\frac{2}{3} \langle \mu_f \rangle^f \left(\frac{1}{r} \frac{\partial}{\partial x_1} \left(r \langle u_1 \rangle^f \right) + \frac{\partial \langle u_2 \rangle^f}{\partial x_2} \right) + 2 \langle \mu_f \rangle^f \frac{\partial \langle u_2 \rangle^f}{\partial x_2} \tag{2.7}$$

$$\langle \tau_{33} \rangle^f = -\frac{2}{3} \langle \mu_f \rangle^f \left(\frac{1}{r} \frac{\partial}{\partial x_1} \left(r \langle u_1 \rangle^f \right) + \frac{\partial \langle u_2 \rangle^f}{\partial x_2} \right) + 2 \langle \mu_f \rangle^f \left(\frac{\langle u_1 \rangle^f}{r} \right) \tag{2.8}$$

where $\langle \mu_f \rangle^f$ is the intrinsic fluid-phase dynamic viscosity and r, u_k and x_k are as denoted previously. Note that in the above, the second coefficient of viscosity is assumed equal to $-2/3 \langle \mu_f \rangle^f$ (Stokes hypothesis).

The body force due to gravity is accounted for via the fluid-phase density varying as an explicit function of temperature. The reason for implementing the aforementioned approach rather than using an approximation such as Boussinesq, is the large variation in the density of gases such as helium resulting from the high temperature gradients inside typical high-temperature reactors. Experimental measurements of the SANA benchmark (as detailed in Section 4.3), show a temperature variation of up to 930 *Kelvin*, corresponding to a factor 2.6 variation in the helium density. Elmo & Cioni [16] indicated that the Boussinesq approximation fails to account for large variations in density, which may lead to the under prediction of velocities generated by the buoyancy effect.

The *energy conservation* equation for the *fluid* phase reads:

$$\frac{\partial}{\partial t}\left(\varepsilon r \langle \rho_f \rangle^f \left\langle C_{p_f} \right\rangle^f \langle T_f \rangle^f\right) + \frac{\partial}{\partial x_j}\left(\varepsilon r \langle \rho_f \rangle^f \left\langle C_{p_f} \right\rangle^f \langle T_f \rangle^f \langle u_j \rangle^f\right) - \frac{\partial}{\partial x_j}\left(\varepsilon r \langle k_f \rangle^f \frac{\partial \langle T_f \rangle^f}{\partial x_j}\right) + \frac{6(1-\varepsilon)}{d_p} r h_{fs}\left(\langle T_f \rangle^f - \langle T_s \rangle^s\right) = 0 \quad (2.9)$$

where $\left\langle C_{p_f} \right\rangle^f$, $\langle k_f \rangle^f$ and $\langle T_f \rangle^f$ are the intrinsic specific heat, thermal conductivity coefficient and temperature of the fluid phase respectively. Further, h_{fs} is the superficial volume-averaged interface heat transfer coefficient between the fluid and solid phase, effectively coupling the respective energy equations, and $\langle T_s \rangle^s$ is the average pebble-surface temperature (in this work assumed to be indicative of the average pebble temperature).

The *energy conservation* of the *solid* phase reads:

$$\frac{\partial}{\partial t}\left((1-\varepsilon) r \langle \rho_s \rangle^s \left\langle C_{p_s} \right\rangle^s \langle T_s \rangle^s\right) - \frac{\partial}{\partial x_j}\left(r k_{eff} \frac{\partial \langle T_s \rangle^s}{\partial x_j}\right) + \frac{6(1-\varepsilon)}{d_p} r h_{fs}\left(\langle T_s \rangle^s - \langle T_f \rangle^f\right) = 0 \quad (2.10)$$

where $\langle C_{p_s} \rangle^s$, $\langle \rho_s \rangle^s$ and k_{eff} respectively are the solid-phase intrinsic specific heat, density and superficial effective thermal conductivity coefficient between the pebbles. Note that h_{fs} and $\langle T_s \rangle^s$ are as defined for the fluid phase energy conservation equation.

2.3 Constitutive Equations

As noted previously, the microscopic flow and heat transfer phenomena present in the pebble bed are accounted for via constitutive equations. These correlations are typically obtained from experimental measurements. The aspects modelled in this way include the porosity distribution ε, solid matrix drag $\mathbf{B}$, fluid-solid interface heat transfer coefficient h_{fs} and effective thermal conductivity k_{eff}. Apart from stating the empirical relations employed, the validity of applying these is rigorously motivated where necessary. This is to ensure the scientific rigour of the work under consideration, which was not done in all instances by others.

2.3.1 Porosity Distribution

The porosity distribution in a packed pebble bed is known to vary when the pebbles are contained by solid walls. This variation, significant close to the vicinity of the wall, has a considerable local effect on the flow (Vortmeyer & Schuster [73]) and heat transfer phenomena as noted by several investigators [13, 47, 56, 69, 76]. A number of experimental [7, 31, 59] and theoretical [27, 28] investigations confirmed that the porosity in beds of randomly packed uniform spheres varies from the limit of 1.0 at the containing walls, to the average bulk porosity of 0.4 in the homogeneous section of the bed. This applies to the radial porosity variation as found in a typical annular reactor structure. If using a comparatively small radial distance over which to average the measured porosity, an oscillatory porosity distribution results (as shown in Figure 2.2). As shown, the wall effect spans a distance of four to five sphere diameters, with the minimum porosity occurring at a distance of half a sphere diameter from the solid wall[1] [7]. Furthermore,

[1] This region is referred to as the near-wall region as explained on page 21.

Benenati & Brosilow [7] observed that the same pattern of oscillations exists in the porosity field regardless of the shape of the bounding surface, be it convex, concave or flat. No information was as yet found though for the porosity distribution characteristics of corners, for example, where the radial and axial boundary effects interact as expected in a typical annular reactor core.

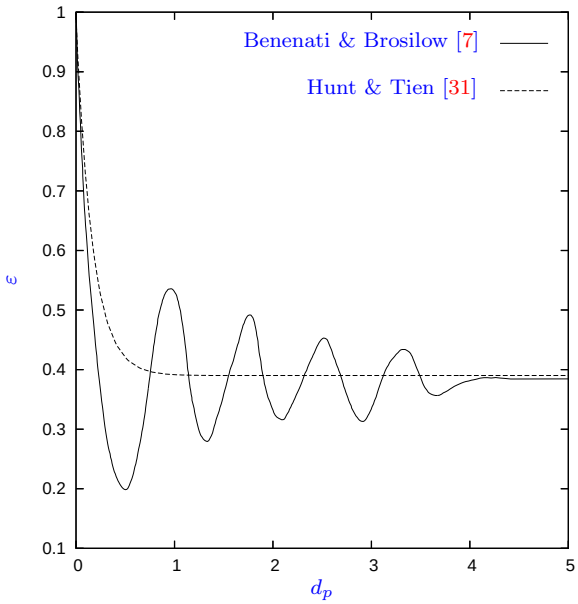

Figure 2.2: Measured (Benenati & Brosilow) radial void fraction distribution for packed beds of uniform spheres contained by a solid wall, as well as the exponential correlation of Hunt & Tien as used in this work. The distance from the solid wall is given in terms of sphere diameters (d_p).

The porosity distribution in this work is calculated as a heterogeneous scalar field, as is fully supported by the governing equations (Section 2.2), and varies between the limits of 0.39 and 0.99. This porosity range is typical of a real-life randomly packed bed[1]. The volume-averaged porosity distribution is calculated using the exponential correlation by Hunt & Tien [31], evaluated and recommended by du Toit [14]. Note that this is a so-called averaged representation of the oscillatory variation in porosity as described above. Figure 2.2 depicts both the

[1]The theoretical upper limit is 1.0, but due to the numerical difficulties arising from using this value (such as devision by zero), it was fixed at 0.99 in this work.

experimentally measured radial porosity distribution of Benenati & Brosilow [7] and a corresponding exponential correlation of Hunt & Tien [31]. Noting that the porosity approaches the limit of 1.0 at the wall, the radial porosity variation is mathematically defined by:

$$\varepsilon(r) = \varepsilon_\infty \left[1 + \frac{1-\varepsilon_\infty}{\varepsilon_\infty} exp\left(-6\frac{r-r_i}{d_p}\right)\right] \quad \forall \quad r_i \leq r \leq \frac{r_i + r_o}{2} \tag{2.11}$$

and

$$\varepsilon(r) = \varepsilon_\infty \left[1 + \frac{1-\varepsilon_\infty}{\varepsilon_\infty} exp\left(-6\frac{r_o-r}{d_p}\right)\right] \quad \forall \quad \frac{r_i + r_o}{2} \leq r \leq r_o \tag{2.12}$$

where ε_∞ is the bulk porosity of the homogeneous packed pebble bed, and r_i and r_o respectively denote the inner and outer radii of the enclosing annular wall. In the case of the packed SANA pebble bed under consideration, ε_∞ is taken as 0.39 [7].

Since the axial length of the reactor modelled (refer to Section 4.3) is not substantially larger than the diameter, the influence of axial porosity variation was considered appreciable in this work. As this results in a two-dimensional porosity field, a method was devised by which to calculate void fraction from the one-dimensional correlations given above. The latter was done by first performing a sweep in both the x_1 and x_2 directions[1], assigning porosity values to the bed area not influenced by wall effects, where the exponential correlation as given by Equations (2.11) and (2.12) was employed. The area covered is indicated in Figure 2.3 by the A-B-C sections, where A represents the homogeneous section of the packed bed. The corner sections (D) represent a square with edge lengths of five times the sphere/particle diameter (the field of influence of two bounding walls). The porosity distribution of the corner sections is now assigned through inverse distance weighting (Watson [74]), using the porosity values as assigned to

[1]Following the observation by Benenati & Brosilow that porosity variations from a flat plate and curved surface display similar behaviour.

the boundaries of the B and C blocks[1] adjacent to the D block. The resulting complete two-dimensional porosity field is as indicated by the contour plot in Figure 2.3. Note that the aforementioned treatment of the corner sections is a simplification due to a lack of relevant information as mentioned earlier.

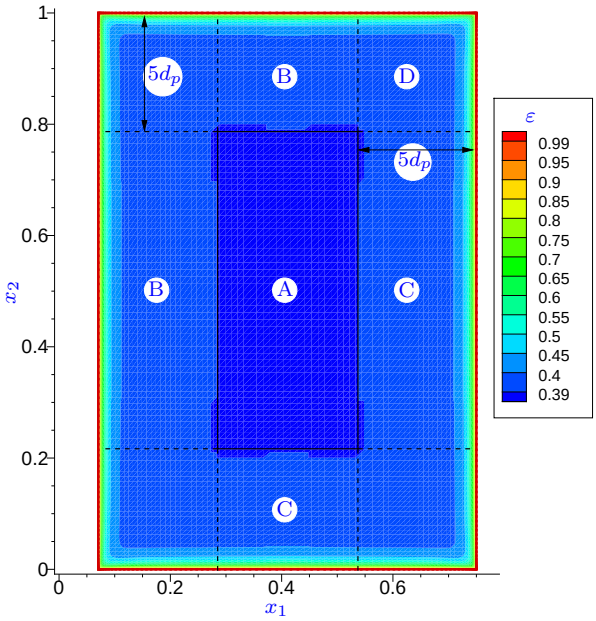

Figure 2.3: Contour plot of the 2-D porosity distribution as applied to the SANA test case.

2.3.2 Solid Matrix Drag Coefficient

The additional fluid drag due to the solid matrix inside a typical reactor, represented in the momentum conservation Equation (2.4) as the vector quantity **B**, is approximated using the vectorial form of the Ergun [17] relation as proposed by Radestock & Jeschar [58]:

[1] On a structured mesh the porosity values assigned to nodes on the boundaries of blocks B and C with either vertical or horizontal spatial coordinates similar to the point in question are used to calculate the final value. The weight of the respective components are determined by their perpendicular distance to the two nearest solid boundaries.

$$B_k = -\left(150\frac{(1-\varepsilon)^2}{\varepsilon}\frac{\langle\mu_f\rangle^f}{{d_p}^2} + 1.75\,(1-\varepsilon)\,\frac{\langle\rho_f\rangle^f}{d_p}\left|\langle\boldsymbol{u}\rangle^f\right|\right)\langle u_k\rangle^f \tag{2.13}$$

where $\langle\mu_f\rangle^f$ is the fluid dynamic viscosity and $\left|\langle\mathbf{u}\rangle^f\right|$ the local intrinsic volume-averaged fluid-phase velocity norm.

As reported by Kuipers *et al.* [40], the vectorial form of the Ergun equation (Equation (2.13)) is valid only for $\varepsilon < 0.8$. The following argument is now presented in an attempt to quantify the result of using the aforementioned relation outside the quoted range of operation because of a lack of suitable alternatives. Note that in this work, the porosity upper limit is taken as 0.99 as stated previously. Considering Equation (2.13), it is noted that apart from the intrinsic fluid material properties $\langle\rho_f\rangle^f$ and $\langle\mu_f\rangle^f$ (which are not affected by porosity variation as a first-order effect), the fluid-phase velocity and porosity variation affect the drag magnitude directly. It is further noted that an increase in porosity and decrease in velocity serve to reduce the magnitude of the drag calculated. The results from modelling the SANA test set-up (Section 4.3) show a maximum vertical fluid-phase velocity of 0.328 m/s (due to wall channelling) for the 5 kW case (Figure 4.7). Considering an extreme case where the vertical velocity distribution through the entire bed is equivalent to this maximum velocity, while allowing the porosity (Figure 4.6) and material properties to be fully variant, a drag distribution results as depicted in Figure 2.4.

From the figure, it is clear that the matrix drag is strongly dependent on the porosity distribution, exponentially tending to zero as the porosity approaches 0.8. The above was done for a constant velocity. In reality, a no-slip viscous boundary condition is applied to all walls, resulting in the velocity approaching zero at the wall (Figure 4.7). This would decrease the magnitude of the calculated drag further. In conclusion, therefore, the magnitude of the matrix drag source term close to a reactor wall should exponentially tend to zero for a varying porosity field as a result of (a) the porosity approaching unity, and (b) the velocity approaching zero close to the wall. Applying the given drag relation for a porosity $\varepsilon > 0.8$ is therefore justified in that the contribution of the drag term to affecting the flow outside of this is believed to be negligible.

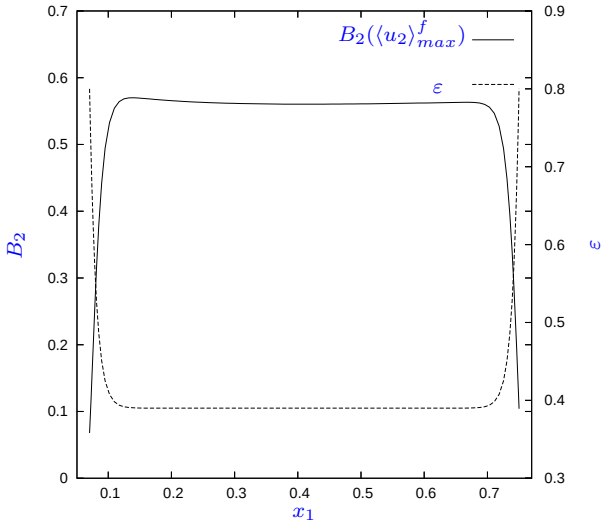

Figure 2.4: Typical porosity distribution (ε) and matrix drag in vertical direction (B_2) based on maximum vertical velocity. The graph is given for the porosity range under which **B** is valid, i.e. $\varepsilon < 0.8$.

2.3.3 Fluid-solid Interface Heat Transfer Coefficient

The interface heat-transfer coefficient h_{fs} (Equations (2.9) and (2.10)) couples the energy conservation equations of the fluid and solid phases, and prescribes the heat transfer between the surface of a representative pebble and the fluid phase. Several correlations for h_{fs} exist, among which are those of Achenbach [1], Gnielinski [26], Gunn [29] and the *Nuclear Safety Standards Commission (KTA)* [39] as used by Gao & Shi [23] and Verkerk [72]. The correlation of Gnielinski is valid for a Reynolds number larger than $500 - 1\,000$ and porosity range of $0.26 < \varepsilon < 1.0$. The KTA correlation is only valid for a statistical/homogeneous pebble-bed, i.e. a porosity range of $0.36 < \varepsilon < 0.42$, and a Reynolds number range of $100 < Re_{d_p} < 10^5$. Achenbach correlated convective heat transfer for a Reynolds number larger than one and a porosity of 0.387. As a result of the stated prevalent flow (buoyancy-driven) and porosity range employed in this work, the correlation considered most suitable is from Gunn, as only this correlation is

valid over the entire range of parameters considered[1]. This relation holds for a porosity range of 0.35 to 1.0, and correlates experimental data for a Reynolds number range of $0 < Re_{d_p} < 10^5$. It follows as:

$$Nu_{d_p} = \left(7 - 10\varepsilon + 5\varepsilon^2\right)\left(1 + 0.7Re_{d_p}^{0.2}Pr^{1/3}\right) + \left(1.33 - 2.4\varepsilon + 1.2\varepsilon^2\right)Re_{d_p}^{0.7}Pr^{1/3} \tag{2.14}$$

where Nu_{d_p}, Pr and Re_{d_p} respectively are the Nusselt, Prandtl and local Reynolds numbers, which are defined as:

$$Nu_{d_p} = \frac{h_{fs}d_p}{\langle k_f \rangle^f}, \quad Pr = \frac{\left\langle C_{pf} \right\rangle^f \langle \mu_f \rangle^f}{\langle k_f \rangle^f}, \quad Re_{d_p} = \frac{\langle \rho_f \rangle^f d_p \varepsilon \left| \langle \boldsymbol{u} \rangle^f \right|}{\langle \mu_f \rangle^f} \tag{2.15}$$

where the nomenclature is as stated previously.

2.3.4 Effective Solid Thermal Conductivity

The effective solid thermal conductivity (k_{eff}) accounts for all non-convective modes of heat transfer within the solid-phase structure. The two correlations widely used [30] are the model of Robold [60] and models based on the original work of Zehner & Schlünder [79]. Semi-empirical versions of the latter type, as evaluated by, among others, Freiwald & Paterson [19], Fundamenski & Gierszewski [21] and Tsotsas & Martin [66], are employed in this work similar to others [6, 15, 40].

The specific form of the effective thermal conductivity applied to the statistical/homogeneous[2] section of the pebble bed is based on the *Zehner-Bauer-Schlünder* (ZBS) correlation, and is detailed by the *International Atomic Energy Agency* (IAEA) [33]. It accounts for the following simultaneous modes of heat transfer:

- Conduction through the solid phase and across the contact interface between pebbles (k_{eff}^{sc}).

[1] Typical Reynolds numbers considered in this work are $Re_{d_p} < 100$, and the porosity range considered is as stated in Section 2.2, i.e. $0.39 < \varepsilon < 0.99$.

[2] Defined as the portion outside the near-wall region.

- Conduction through the solid phase and radiation between pebbles (k_{eff}^{sr}).
- Conduction through the solid phase and across the stationary fluid phase filling the interstitial voids between the pebbles (k_{eff}^{sf}).

The component of the effective thermal conductivity which describes conduction through the pebbles and across the contact between the pebbles is given by:

$$\frac{k_{eff}^{sc}}{\langle k_s \rangle^s} = \left(\frac{3\left(1-\epsilon^2\right)}{4E_s} \frac{f d_p}{2} \right)^{1/3} \frac{1}{0.531S} \left(\frac{N_A}{N_L} \right) \tag{2.16}$$

where

$$f = p_s \frac{S_F}{N_A} \tag{2.17}$$

while $N_A = 1/d_p^2$ and $N_L = 1/d_p$ denote the number of particles per unit area and length respectively, while $S = 1$ and $S_F = 1$ are constants related to the volumetric arrangement of the pebbles [36]. Further, $\langle k_s \rangle^s$ is the solid-phase thermal conductivity and $E_s = 9.0 \times 10^9 N/m^2$ and $\epsilon = 0.136$ denote the solid-phase Young's modules and Poisson's ratio respectively (for carbon pebbles as used in reactors). The form factor f ($f = 59.8$ in this work [33]) accounts for heat transfer effects as a result of pebble deformation due to the accumulated weight of the pebbles in the bed. The external pressure as a result of the stacked pebbles is denoted by p_s.

The effective thermal conductivity accounting for interstitial void radiation and solid conduction is given by the Zehner-Schlünder equation as modified by Breitbach & Barthels [10]:

$$k_{eff}^{sr} = \left(\left[1 - (1-\varepsilon)^{1/2} \right] \varepsilon + \frac{(1-\varepsilon)^{1/2}}{2/\xi_s - 1} \frac{\beta + 1}{\beta} \frac{1}{1 + \frac{1}{(2/\xi_s - 1)\Psi}} \right) 4\sigma (\langle T_s \rangle^s)^3 d_p \tag{2.18}$$

where

$$\beta = 1.25 \left(\frac{1-\varepsilon}{\varepsilon} \right)^{10/9} \tag{2.19}$$

and

$$\Psi = \frac{\langle k_s \rangle^s}{4\sigma(\langle T_s \rangle^s)^3 d_p} \tag{2.20}$$

Here, ξ_s denotes the pebble emissivity ($\xi_s = 0.8$ in this work) and σ the Stephan-Boltzmann constant ($\sigma \simeq 5.67 \times 10^{-8}\ W/m^2K^4$). Also, β is the deformation factor and Ψ forms part of *Damköhler's* equivalent thermal conductivity [5] describing the radiative heat transfer.

The final component of the effective thermal conductivity accounts for thermal conduction within the interstitial voids filled by the gas as well as the pebble solid conduction. This is given by:

$$\frac{k_{eff}^{sf}}{\langle k_f \rangle^f} = 1 - \sqrt{1-\varepsilon} + \frac{2\sqrt{1-\varepsilon}}{1-\kappa\beta}\left[\frac{(1-\kappa)\beta}{(1-\kappa\beta)^2} ln\left(\frac{1}{\kappa\beta}\right) - \frac{\beta+1}{2} - \frac{\beta-1}{1-\kappa\beta}\right] \tag{2.21}$$

where β is the same as in Equation (2.19) and the conductivity ratio is given by $\kappa = \langle k_f \rangle^f / \langle k_s \rangle^s$. The aforementioned correlation (Equation (2.21)) was evaluated by Prasad *et al.* [55] and found to be satisfactory for a conductivity ratio smaller than unity (the maximum conductivity ratio seen in this work is 0.013).

The above correlations may now be combined to obtain an expression for the total effective conductivity of the homogeneous section of the packed pebble bed as:

$$k_{eff}^H = k_{eff}^{sr} + k_{eff}^{sf} + k_{eff}^{sc} \tag{2.22}$$

The exclusivity of the above relation for k_{eff}^H (*Zehner-Bauer-Schlünder*[1] model) to a homogeneous bed is due to conflicting reports as to its validity in the near-wall region[2]. Considering the respective components of k_{eff}^H (Equation (2.22)), it is noted that the mathematical correlation for the radiative component (k_{eff}^{sr}, Equation (2.18)) is problematic as it exponentially approaches infinity as porosity approaches one. Bauer & Schlünder [5] noted that the increase in porosity due

[1]The so-called *Zehner-Bauer-Schlünder* (ZBS) model as referred to in [33, 64] refers to a correlation which is based on the original work of Zehner & Schlünder [79].

[2]The near-wall region is defined as the distance from the wall to the midpoints of the pebbles in contact with the wall. In this region, the porosity dramatically increases to the theoretical limit of one at the wall.

to a solid wall[1], results in a decrease in the number of contact points between pebbles, which in turn affects the radiation and conduction heat transfer components. They concluded, however, that the two modes of heat transfer are of the same order of magnitude but inverse in change, and therefore the effect of porosity can be disregarded. No quantitative values are given to clearly substantiate this though. Further, it is noted by Thurgood *et al.* [64] and the *IAEA* [33] that the *ZBS* model can only be applied meaningfully to a homogeneous bed. The former authors [64] noted that applying the *ZBS* model in the near-wall region, where the porosity dramatically increases, results in a non-physical infinite thermal conductivity as the void fraction approaches one. This was also the finding of the author of this thesis.

To overcome the aforementioned problem, the modified *ZBS* model as proposed by Tsotsas [65] is employed to calculate the effective thermal conductivity in the near-wall region (denoted k_{eff}^{nw}). The modified model requires the recalculation of the radiative component, i.e.

$$k_{eff}^{nw} = k_{eff}^{sr}\Big|^{nw} + k_{eff}^{sf} + k_{eff}^{sc} \tag{2.23}$$

where k_{eff}^{sf} and k_{eff}^{sc} are as defined before, and $k_{eff}^{sr}\Big|^{nw}$ is the modified radiative component calculated as:

$$k_{eff}^{sr}\Big|^{nw} = \left(1-\sqrt{1-\varepsilon}\right)\varpi_R + \sqrt{1-\varepsilon}\left(\frac{1}{\varpi_R} + \frac{1}{1/\kappa}\right)^{-1} \tag{2.24}$$

where

$$\varpi_R = \frac{4\sigma}{2/\xi_s - 1}(\langle T_s\rangle^s)^3 \frac{d_p}{\langle k_f\rangle^f} \tag{2.25}$$

The conductivity ratio κ and ξ_s are as defined previously, while ϖ_R is the radiative component.

Thurgood *et al.* [64] noted, however, that the above model for k_{eff}^{nw} is not continuous with the parent correlation (k_{eff}^{H}) which is to be applied to the homogeneous section of the bed. This is shown graphically in Figure 2.5, where both correlations are plotted at a horizontal section through the bed for the two

[1]No upper limit of porosity was stated in this paper though.

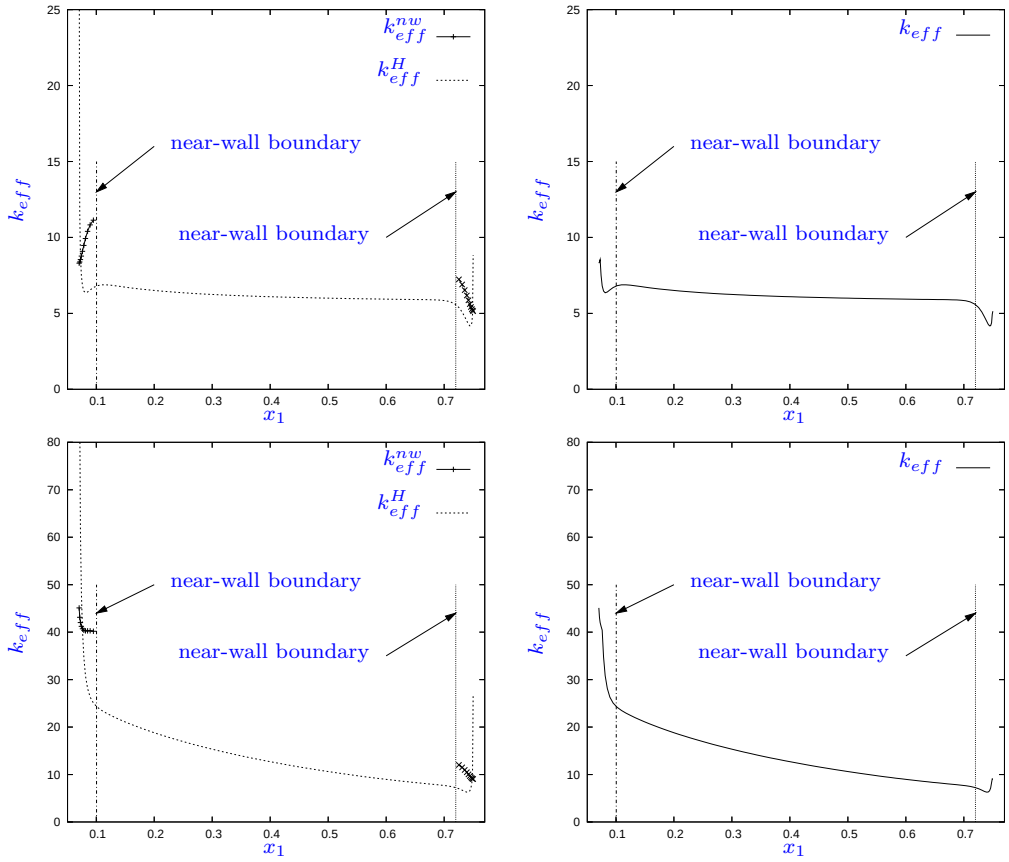

Figure 2.5: Modified ZBS correlation (k_{eff}^{nw}) and effective thermal conductivity, based on the original model by Zehner & Schlünder [79] (k_{eff}^{H}), calculated at a section through the vertical centreline for the 5 kW (top left) and 35 kW (bottom left) SANA test cases. The final values of k_{eff} employed in this work for the respective test cases are shown on the right-hand side.

SANA test cases considered. Note that the vertical axis is capped as the value for k_{eff}^{H} tends to infinity as the wall is approached (where the porosity approaches the limit of one). Further note the discontinuous jump between the k_{eff}^{nw} and k_{eff}^{H} correlations on the edge of the near-wall regions.

Considering the aforementioned, and the unavailability of reputable alternative correlations, an approximation is proposed in order to realise an orderly accurate relation for k_{eff} over the entire porosity range: Apart from calculating

k_{eff}^{H} for the homogeneous section of the packed bed, both k_{eff}^{nw} and k_{eff}^{H} are to be calculated in the near-wall region. The smaller of the aforementioned two models in the near-wall region would then determine the final value assigned to the effective thermal conductivity, simply denoted k_{eff}. The aforementioned signifies that the smaller of k_{eff}^{sr} and $k_{eff}^{sr}\big|^{nw}$ determines the radiative component to be added to k_{eff} in the near-wall region. This serves the dual purpose of preventing the effective thermal conductivity from becoming infinite as well as reducing the level of discontinuity between k_{eff}^{H} and k_{eff}^{nw} (as shown in Figure 2.5). The aforementioned may be expressed mathematically as follows:

$$k_{eff} = \begin{cases} k_{eff}^{H} & \forall \quad \varepsilon \leq 0.42 \\ min\left(k_{eff}^{H}, k_{eff}^{nw}\right) & \forall \quad \varepsilon > 0.42 \end{cases} \tag{2.26}$$

where $\varepsilon = 0.42$ denotes the porosity corresponding to the start of the near-wall region.

2.4 Material Properties

The two phases (fluid and solid) considered in this work (Section 4.3) constitute helium and non-irradiated graphite of type Sigri AL $2-500$[1] respectively. The temperature-dependent material properties used for helium are as prescribed by the *Nuclear Safety Standards Commission* [38], while the material properties for the graphite were referenced from the *International Atomic Energy Agency* [33] and Niessen & Stöcker [51]. These are documented in detail in Appendix A.

2.5 Boundary Conditions

Boundary conditions applied at domain boundaries are of both Dirichlet and Neumann types. The former includes fluid no-slip conditions as well as prescribed temperatures for the fluid and solid phases. The Neumann conditions involve adiabatic as well as heat flux. The former for an arbitrary phase ψ reads:

[1] These are similar to substances used in high-temperature gas-cooled nuclear reactors.

$$\frac{\partial \langle T_\psi \rangle^\psi}{\partial x_j} n_j = 0 \quad \forall \quad \mathbf{x} \in \mathcal{A}_\psi \tag{2.27}$$

where $\mathcal{A}_\psi$ denotes where the boundary surface intersects with phase ψ.

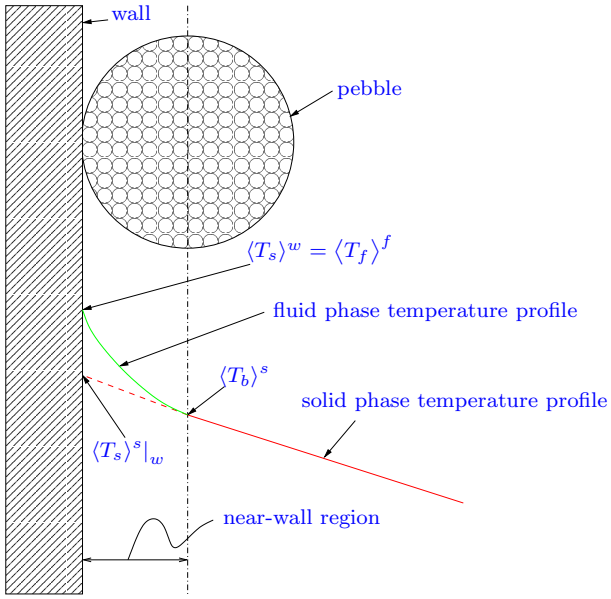

Figure 2.6: Schematic diagram of the variables involved in calculating the heat flux Neumann boundary condition. In the figure, $\langle T_s \rangle^s|_w$ and $\langle T_s \rangle^w$ denote the pebble temperature at the wall and actual wall temperature respectively.

As was noted by Amiri *et al.* [2], implementing a wall heat-flux boundary condition when using a two-equation energy model (local thermal disequilibrium or pseudo-heterogeneous model as defined on page 8), is not straightforward while rigorous formulations of such a boundary condition are scarce. Therefore, a constant heat-flux boundary condition mathematical formulation, which is suitable for numerical discretisation, is proposed in this work. This is detailed next. In this work the fluid-phase temperature is assumed representative of the actual wall temperature at the bed-wall boundary. This is as a realistic porosity variation with upper bound 0.99 is employed at the wall. With reference to Figure 2.6, the heat influx to the solid phase is now prescribed with a radiative-type boundary condition from the model of Schlünder, as documented by Fundamenski & Gierszewski [20, 21]:

$$q_{solid} = -k_{eff}\frac{\partial \langle T_s \rangle^s}{\partial x_j} n_j = h_r \left((\langle T_s \rangle^w)^4 - (\langle T_b \rangle^s)^4 \right) \tag{2.28}$$

with $\langle T_s \rangle^w = \langle T_f \rangle^f$ and

$$h_r = \sigma \left[\frac{1}{\xi_s} + \frac{1}{\xi_w} - 1 \right]^{-1} \tag{2.29}$$

where ξ_s and ξ_w are the emissivity of the solid phase and wall respectively (taken as $\xi_s = 0.8$ and $\xi_w = 0.6$ in this work[1]) and $\langle T_b \rangle^s$ denotes the solid-phase temperature on the edge of the near-wall region as shown. Here, $\langle T_b \rangle^s$ is calculated by extrapolating linearly from the wall to a distance of half a sphere diameter into the bed in a direction perpendicular to the wall as:

$$\langle T_b \rangle^s \approx \left(\frac{\partial \langle T_s \rangle^s}{\partial x_k}\bigg|_w n_k \right) \left(-\frac{d_p}{2} \right) + \langle T_s \rangle^s|_w \tag{2.30}$$

where the subscript w indicates property values at the wall and $\mathbf{n}$ is the outward-pointing unit vector normal to the wall. It is important to note that $\langle T_b \rangle^s$ is to be calculated via the proposed relation, as it is not explicitly solved for, whereas the $\langle T_s \rangle^s$ field is calculated.

The fluid-phase heat flux is now calculated in a manner which enforces a specified heat flux as:

$$q_{fluid} = -\varepsilon \langle k_f \rangle^f \frac{\partial \langle T_f \rangle^f}{\partial x_j} n_j = q_{input} - q_{solid} \tag{2.31}$$

where q_{input} is the prescribed heat flux, and q_{solid} the heat flux as calculated in Equation (2.28).

Considering contact resistance at the interface between the solid wall and working fluid (interfacial conductance h_w), which accounts for the inhibition of heat transfer at the wall due to a layer of unmixed fluid, Tsotsas & Schlünder [67] noted and Freiwald & Paterson [19] confirmed that considerable scatter is present in the heat transfer coefficients predicted by the various models in existence. Furthermore, it was pointed out by Tsotsas & Schlünder that the wall heat-transfer coefficient h_w need not be accounted for when the Reynolds number

[1] The chosen values for ξ_s and ξ_w are for use with the SANA test case. See Chapter 4.

(Re_{d_p}) is smaller than 100[1], as the resistance to heat transfer is then considered negligible. As a result of the aforementioned, the effect of a "contact resistance" on the influx of heat from the reactor wall is not considered in this work, lending further credibility to the assumption $\langle T_s \rangle^w = \langle T_f \rangle^f$.

2.6 Conclusion

This chapter detailed the mathematical description of the conservation laws required to describe fluid flow and heat transfer through randomly packed pebble beds. The latter was via a continuum approach where two phases are considered, viz. a fluid and solid phase. The actual governing equations were documented and the constitutive equations formulated and rigorously motivated. Finally, boundary condition formulations, which both complement the governing equations employed and are suitable for numerical discretisation, are proposed.

[1]The maximum Reynolds number considered in this work is less than 100.

Chapter 3

Solution Procedure

3.1 Introduction

The governing equations employed in this work constitute a formidably complex set of highly non-linear strongly coupled partial differential equations. Obtaining a general solution via analytical means is therefore at present an impossibility, and a numerical solution method is sought. The latter requires the discretisation, both spatially and temporal, of the governing equation set presented.

In describing the solution procedure, it is instructive to write the system of governing equations in the following form:

$$\frac{\partial \boldsymbol{W}}{\partial t} + \frac{\partial \boldsymbol{F}^j}{\partial x_j} - \frac{\partial \boldsymbol{G}^j}{\partial x_j} + r\varepsilon \frac{\partial \boldsymbol{H}}{\partial x_j} = \boldsymbol{S} \tag{3.1}$$

where

$$\boldsymbol{W} = \begin{pmatrix} r\varepsilon \langle \rho_f \rangle^f \\ r\varepsilon \langle \rho_f \rangle^f \langle u_1 \rangle^f \\ r\varepsilon \langle \rho_f \rangle^f \langle u_2 \rangle^f \\ r\varepsilon \langle \rho_f \rangle^f \left\langle C_{p_f} \right\rangle^f \langle T_f \rangle^f \\ r(1-\varepsilon) \langle \rho_s \rangle^s \left\langle C_{p_s} \right\rangle^s \langle T_s \rangle^s \end{pmatrix} \quad ; \quad \boldsymbol{F}^j = \begin{pmatrix} r\varepsilon \langle \rho_f \rangle^f \langle u_j \rangle^f \\ r\varepsilon \langle \rho_f \rangle^f \langle u_1 \rangle^f \langle u_j \rangle^f \\ r\varepsilon \langle \rho_f \rangle^f \langle u_2 \rangle^f \langle u_j \rangle^f \\ r\varepsilon \langle \rho_f \rangle^f \left\langle C_{p_f} \right\rangle^f \langle T_f \rangle^f \langle u_j \rangle^f \\ 0 \end{pmatrix} \tag{3.2}$$

$$\boldsymbol{G}^j = \begin{pmatrix} 0 \\ r\varepsilon \langle \tau_{1j} \rangle^f \\ r\varepsilon \langle \tau_{2j} \rangle^f \\ r\varepsilon \langle k_f \rangle^f \frac{\partial \langle T_f \rangle^f}{\partial x_j} \\ r k_{eff} \frac{\partial \langle T_s \rangle^s}{\partial x_j} \end{pmatrix} \qquad \boldsymbol{H} = \begin{pmatrix} 0 \\ \langle p \rangle^f \delta_{1j} \\ \langle p \rangle^f \delta_{2j} \\ 0 \\ 0 \end{pmatrix} \tag{3.3}$$

and

$$\boldsymbol{S} = \begin{pmatrix} 0 \\ r\varepsilon \langle \rho_f \rangle^f g_1 + rB_1 - (1 - \delta_{1\zeta}) \varepsilon \langle \tau_{33} \rangle^f \\ r\varepsilon \langle \rho_f \rangle^f g_2 + rB_2 \\ -r(1-\varepsilon) \frac{6}{d_p} h_{fs} \left(\langle T_f \rangle^f - \langle T_s \rangle^s \right) \\ -r(1-\varepsilon) \frac{6}{d_p} h_{fs} \left(\langle T_s \rangle^s - \langle T_f \rangle^f \right) \end{pmatrix} \tag{3.4}$$

where the nomenclature is as defined previously and $j = 1, 2$.

3.2 Artificial Compressibility

Equation (3.1) is numerically problematic when applied to low Mach number or incompressible flows. This is due to the large disparity between the acoustic and convective velocities resulting in an extremely stiff system. *Artificial compressibility* was introduced by Chorin [11], which entails a method of solving the aforementioned problem through the introduction of an artificial relation between density and pressure. This technique was employed in this work as it inherently allows for matrix free solution (memory efficient) and its natural suitability to parallel environments, while allowing for the mutual technology transfer with compressible time-marching solvers [46].

To apply the artificial relation between density and pressure in a consistent manner, the locally generalised preconditioned artificial compressibility version (Malan *et al.* [46]) is extended in this work. This is done by additionally accounting for temporal variations in the fluid material properties (due to temperature variations) as follows:

$$\frac{\partial \mathbf{W}}{\partial \mathbf{Q}}\frac{\partial \mathbf{Q}}{\partial t_\tau} + \frac{\partial \mathbf{F}^j}{\partial x_j} - \frac{\partial \mathbf{G}^j}{\partial x_j} + r\varepsilon\frac{\partial \mathbf{H}}{\partial x_j} = \mathbf{S} \tag{3.5}$$

where

$$\frac{\partial \mathbf{W}}{\partial \mathbf{Q}} = \tag{3.6}$$

$$\begin{pmatrix} \frac{r\varepsilon}{c_{\tau cont-mom}^2} & 0 & 0 & 0 & 0 \\ \frac{a_u r\varepsilon \langle u_1 \rangle^f}{c_{\tau cont-mom}^2} & r\varepsilon \langle \rho_f \rangle^f & 0 & 0 & 0 \\ \frac{a_u r\varepsilon \langle u_2 \rangle^f}{c_{\tau cont-mom}^2} & 0 & r\varepsilon \langle \rho_f \rangle^f & 0 & 0 \\ \frac{a_T r\varepsilon \langle C_{p_f} \rangle^f \langle T_f \rangle^f}{c_{\tau cont-mom}^2} & 0 & 0 & r\varepsilon \langle \rho_f \rangle^f \left\langle C_{p_f} \right\rangle^f & 0 \\ 0 & 0 & 0 & 0 & r(1-\varepsilon) \langle \rho_s \rangle^s \langle C_{p_s} \rangle^s \end{pmatrix}$$

and

$$\mathbf{Q} = \begin{pmatrix} \langle p \rangle^f \\ \langle u_1 \rangle^f \\ \langle u_2 \rangle^f \\ \langle T_f \rangle^f \\ \langle T_s \rangle^s \end{pmatrix} \tag{3.7}$$

Further,

$$a_T = \begin{cases} 0 & \text{if} \quad a_u = 0 \\ 1 & \text{if} \quad a_u > 0 \end{cases} \tag{3.8}$$

and a_u is calculated in the interests of stability and convergence performance as per Malan *et al.* [46]. As the introduction of artificial compressibility destroys the temporal accuracy of the given equation (which may be recovered via a dual-stepping procedure [63]), time is replaced with pseudo-time t_τ. The pseudo-acoustic velocity $c_{\tau cont-mom}$, which is related to the maximum eigenvalue of the continuity and momentum conservation equations, is calculated from the following relation

$$c_{\tau cont-mom} = max\left(c_{\tau conv}, c_{\tau diff}\right) \tag{3.9}$$

where the convective acoustic velocity $c_{\tau conv}$ is calculated as per [46]:

$$c_{\tau conv} = \begin{cases} \varepsilon_{c_{\tau conv}} & \text{if} \quad \left|\langle \boldsymbol{u} \rangle^f\right| \leq \varepsilon_{c_{\tau conv}} \\ \left|\langle \boldsymbol{u} \rangle^f\right| & \text{if} \quad \left|\langle \boldsymbol{u} \rangle^f\right| > \varepsilon_{c_{\tau conv}} \end{cases} \tag{3.10}$$

where $\left|\langle \boldsymbol{u} \rangle^f\right| = \sqrt{\langle u_j \rangle^f \langle u_j \rangle^f}$ and $\varepsilon_{c_{\tau conv}}$ is typically set to $10^{-5} \left|\langle \boldsymbol{u} \rangle^f\right|_{max}$ with $\left|\langle \boldsymbol{u} \rangle^f\right|_{max}$ being the maximum velocity magnitude in the field. The diffusive component is determined by a relation which takes into consideration only the viscous diffusion velocity as:

$$c_{\tau diff} = \frac{\langle \mu_f \rangle^f}{\langle \rho_f \rangle^f \Delta\chi \sigma_{vn}} + \left|\langle \boldsymbol{u} \rangle^f\right| \tag{3.11}$$

In the above relation, $\Delta\chi$ denote the local spatial discretisation size (effective cell/element size). Further, σ_{vn} is the von Neumann number, which is typically set to 0.1 in this work in the interest of generic stability. Note that as stated in Section 2.2, the intrinsic volume-averaged fluid viscosity $\langle \mu_f \rangle^f$ may vary by a factor 2.6 or more over the computational domain.

3.3 Spatial Discretisation

In this work, a vertex-centred edge-based finite volume algorithm is used for the purposes of spatial discretisation. This method of discretisation is advantageous in terms of computational efficiency and applicability to hybrid-unstructured meshes (Malan [45]), while allowing more direct application of certain boundary conditions as compared to the cell-centered finite volume method. Furthermore, a compact stencil method is employed for diffusive terms in the interests of both stability and accuracy (Lewis & Malan [43]). The first step in discretising the system of governing equations is subdivision of the solution spatial domain $\mathcal{V}$ into non-overlapping volumes $\mathcal{V}_\zeta \in \mathcal{V}$, and application of the system of governing equations to each volume or sub-domain in weak form. The sub-domains are constructed on the mesh as per Vahdati *et al.* [70]. In 2D, this involves connecting edge midpoints and element centroids such that only one node is present in each control volume. This is shown schematically for a node m in Figure 3.1. The

volume (sub-domain) associated with node m is designated $\mathcal{V}_m$ and the bounding surface $\mathcal{A}_m$.

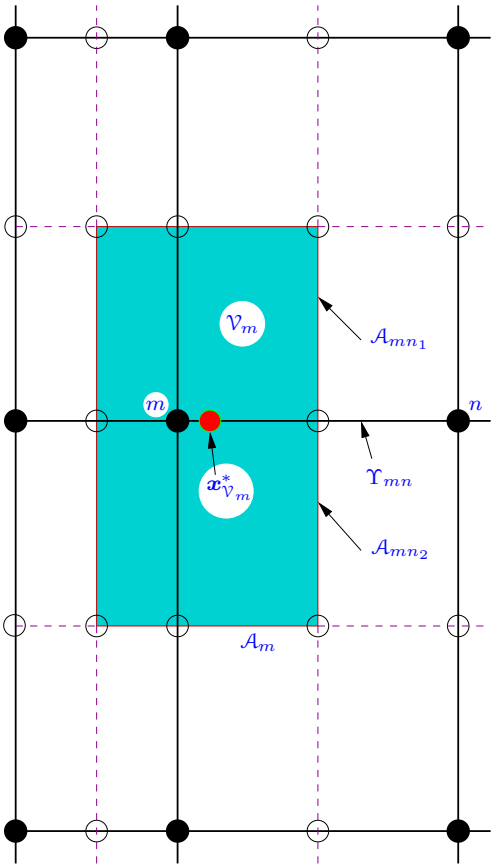

Figure 3.1: Schematic diagram of the construction of the median dual-mesh on a stretched grid. The volume-averaged centroid position of volume $\mathcal{V}_m$ is indicated by $\boldsymbol{x}^*_{\mathcal{V}_m}$, and Υ_{mn} depicts the edge connecting nodes m and n.

In the light of the above, the governing equation set (Equation (3.5)), after application of the Divergence theorem, follows as:

$$\int_{\mathcal{V}_\zeta} \frac{\partial \boldsymbol{W}}{\partial \boldsymbol{Q}} \frac{\partial \boldsymbol{Q}}{\partial t_\tau} d\mathcal{V} + \int_{\mathcal{A}_\zeta} \left(\boldsymbol{F}^j - \boldsymbol{G}^j + \overline{r}_{\mathcal{V}_\zeta} \overline{\varepsilon}_{\mathcal{V}_\zeta} \boldsymbol{H} \right) n_j d\mathcal{A} = \int_{\mathcal{V}_\zeta} \boldsymbol{S} d\mathcal{V} \tag{3.12}$$

where $\mathcal{A}_\zeta$ is the surface bounding $\mathcal{V}_\zeta$ and $\mathbf{n}$ is the unit vector in the direction normal to the boundary segment $d\mathcal{A}$. Further, $\overline{r}_{\mathcal{V}_\zeta}$ and $\overline{\varepsilon}_{\mathcal{V}_\zeta}$ respectively are the

spatially integrated average radius and porosity with respect to $\mathcal{V}_\zeta$. Note that particularly at boundary nodes, this is typically very different from the value at the node (vertex) itself (an example of the aforementioned is indicated in Figure 3.1 for the first non-boundary node m). In this work, $\overline{r}_{\mathcal{V}_m}$ and $\overline{\varepsilon}_{\mathcal{V}_m}$ are calculated in a generically applicable manner (arbitrary volumes) by evaluation at the geometric centroid of the volume viz. $\overline{r}_{\mathcal{V}_m} \approx r(\boldsymbol{x}^*_{\mathcal{V}_m})$ and $\overline{\varepsilon}_{\mathcal{V}_m} \approx \varepsilon(\boldsymbol{x}^*_{\mathcal{V}_m})$. Here, $\boldsymbol{x}^*_{\mathcal{V}_m}$ is determined by triangulating the latter into volumes $\mathcal{V}_{\zeta_k}$, and computing as

$$\boldsymbol{x}^*_{\mathcal{V}_m} = \frac{\sum_k \mathcal{V}_{\zeta_k} \boldsymbol{x}^*_{\mathcal{V}_{\zeta_k}}}{\sum_k \mathcal{V}_{\zeta_k}} \tag{3.13}$$

where $\boldsymbol{x}^*_{\mathcal{V}_{\zeta_k}}$ is the geometric centroid of $\mathcal{V}_{\zeta_k}$.

All surface integrals are calculated in an edge-wise manner. For this purpose, bounding surface information is similarly stored in an edge-wise manner and termed *edge-coefficients*. The latter, for a given internal edge connecting nodes m and n, is defined as

$$\boldsymbol{C}_{mn} = \boldsymbol{n}^{mn_1} \mathcal{A}_{mn_1} + \boldsymbol{n}^{mn_2} \mathcal{A}_{mn_2} \tag{3.14}$$

where $\mathcal{A}_{mn_1}$ is a bounding-surface segment intersecting the edge (Figure 3.1). The discrete form of the surface integral in Equation (3.12), computed for the volume surrounding the node m, now follows as

$$\int_{\mathcal{A}_\zeta} \left(\boldsymbol{F}^j - \boldsymbol{G}^j + \overline{r}_{\mathcal{V}_m} \overline{\varepsilon}_{\mathcal{V}_m} \boldsymbol{H}\right) n_j d\mathcal{A} \approx \sum_{\Upsilon_{mn} \cap \mathcal{V}_m} \left(\boldsymbol{F}^j_{\overline{f}_{mn}} - \left[\boldsymbol{G}^j_{\overline{f}_{mn}}\Big|_{tang} + \boldsymbol{G}^j_{\overline{f}_{mn}}\Big|_{norm} \right] + \overline{r}_{\mathcal{V}_m} \overline{\varepsilon}_{\mathcal{V}_m} \overline{\boldsymbol{H}}_{mn} \right) C^j_{mn} \tag{3.15}$$

where all $\overline{\bullet}_{mn}$ quantities denote edge-averaged values, and the operator f returns the latter such that second-order accuracy of the overall scheme is ensured (Lewis & Malan [43]):

$$\overline{f}_{\Upsilon_{mn}} = f\left(\overline{r}_{mn}, \overline{\varepsilon}_{mn}, \overline{\langle u_j \rangle^f}_{mn}, \overline{\langle T_f \rangle^f}_{mn}, \overline{\langle T_s \rangle^s}_{mn}\right) \tag{3.16}$$

Further, $\boldsymbol{G}^j|_{tang}$ is calculated by employing directional derivatives and $\boldsymbol{G}^j|_{norm}$ is approximated by employing the standard finite volume first-order derivative terms.

The temporal term is spatially discretised at a node m as

$$\int_{\mathcal{V}_m} \frac{\partial \boldsymbol{W}}{\partial \boldsymbol{Q}} \frac{\partial \boldsymbol{Q}}{\partial t_\tau} d\mathcal{V} \approx \left.\frac{\partial \boldsymbol{W}}{\partial \boldsymbol{Q}}\right|_{\overline{g}_m} \frac{\partial \boldsymbol{Q}_m}{\partial t_\tau} \mathcal{V}_m \tag{3.17}$$

where the Jacobian is evaluated at $\overline{g}_m = \left(r(\boldsymbol{x}^*_{\mathcal{V}_m}), \varepsilon(\boldsymbol{x}^*_{\mathcal{V}_m}), \langle u_j \rangle^f_m, \langle T_f \rangle^f_m\right)$. The source term $\boldsymbol{S}$ is discretised in a similar manner, from which the following spatially discretised governing equation results at a node m:

$$\left.\frac{\partial \boldsymbol{W}}{\partial \boldsymbol{Q}}\right|_{\overline{g}_m} \frac{\partial \boldsymbol{Q}_m}{\partial t_\tau} \mathcal{V}_m = \sum_{\Upsilon_{mn} \cap \mathcal{V}_m} \left(\boldsymbol{F}^j_{\overline{f}_{mn}} - \left[\boldsymbol{G}^j_{\overline{f}_{mn}}\Big|_{tang} + \boldsymbol{G}^j_{\overline{f}_{mn}}\Big|_{norm} \right] + \overline{r}_{\mathcal{V}_m} \overline{\varepsilon}_{\mathcal{V}_m} \overline{\boldsymbol{H}}_{mn} \right) C^j_{mn} + \boldsymbol{S}_{\overline{g}_m} \mathcal{V}_m \tag{3.18}$$

where the nomenclature is as defined above.

3.4 Stabilisation

Due to the central difference nature of the chosen spatial discretisation scheme, stabilisation is required where convective terms are involved to eliminate spurious oscillations. The decision as to the appropriate stabilisation scheme to employ, was done based on an evaluation of three methods. To this end, first order accurate upwinding, artificial dissipation and a characteristic based method were evaluated in terms of accuracy and robustness. The *one-dimensional linear advection-diffusion equation* was chosen to evaluate the aforementioned stabilisation schemes, as it consists of both *convective* (advection) and *diffusive* components. This is similarly the case with the volume-averaged governing equations dealt with in this work (Section 2.2).

The one-dimensional advection-diffusion equation, written for a one-dimensional spatial domain $\mathcal{V} = [0; \mathcal{L}]$, is given by:

$$\frac{\partial \phi}{\partial t} + u_1 \frac{\partial \phi}{\partial x_1} - \alpha \frac{\partial^2 \phi}{\partial x_1^2} = 0 \quad \forall \quad x_1 \in [0; \mathcal{L}], \quad t \in \mathcal{I} \tag{3.19}$$

where the dependent variable is ϕ, and has continuous derivatives at each point within $\mathcal{V}$. Furthermore, u_1 and α are constant, and $\mathcal{I}$ denotes the temporal domain.

The model problem, based on the above, consists of a prescribed thermal diffusivity α over the spatial domain $\mathcal{V}$, as well as Dirichlet-type boundary conditions as follows:

$$\begin{aligned} \phi &= \Phi_L \qquad \text{at} \qquad x_1 = 0 \\ \phi &= \Phi_R \qquad \text{at} \qquad x_1 = \mathcal{L} \end{aligned} \tag{3.20}$$

The exact solution to the steady form of Equation (3.19) is given by:

$$\frac{\phi - \Phi_L}{\Phi_R - \Phi_L} = \frac{\exp\left(\frac{Pe}{\mathcal{L}} x_1\right) - 1}{\exp\left(Pe\right) - 1} \tag{3.21}$$

where the Peclet number is calculated as $Pe = u_1 \mathcal{L}/\alpha$ and gives the ratio between the convective- and global diffusive velocities of information propagation viz. u_1 and $\alpha/\mathcal{L}$, where the nomenclature is as defined previously.

3.4.1 Numerical Discretisation

By employing the methodology described in Section 3.3, the one-dimensional advection-diffusion equation is discretized at a non-boundary node m as follows:

$$\frac{\phi_m^{t+\Delta t} - \phi_m^t}{\Delta t} + \frac{1}{\mathcal{V}_m} \sum_{\Upsilon_{mn} \cap \mathcal{V}_m} u_1 \overline{\phi}_{mn}^t C_{mn}^1 - \frac{\alpha}{\mathcal{V}_m} \sum_{\Upsilon_{mn} \cap \mathcal{V}_m} \frac{(\phi_n^t - \phi_m^t)}{l_{mn}} t_{mn}^1 C_{mn}^1 \approx 0 \tag{3.22}$$

where the superscript t refers to conditions at the current time level, Δt is the allowable time-step size, t_{mn}^1 is the component of the unit vector parallel to the edge connecting nodes m and n in the x_1 direction, and the remainder of the nomenclature is as previously defined. Equation (3.22) is notionally second-order accurate in space, and since a steady-state solution is sought, temporal accuracy is of no concern. The allowable time-step size, calculated to furnish a stable and efficient solution process, is given by:

$$\Delta t = \frac{CFL}{\left(\frac{u_1}{\Delta x_1} + 2\frac{\alpha}{(\Delta x_1)^2}\right)} \tag{3.23}$$

where CFL[1] ≤ 1 to ensure a stable solution process.

Equation (3.22) is susceptible to non-physical oscillations (as pointed out previously). This may be dealt with via the addition of a stabilizing term $\mathcal{D}$ to the right-hand-side, and such that the following equation results at a node m:

$$\frac{\phi_m^{t+\Delta t} - \phi_m^t}{\Delta t} + \frac{1}{\mathcal{V}_m} \sum_{\Upsilon_{mn} \cap \mathcal{V}_m} u_1 \overline{\phi}_{mn}^t C_{mn}^1 - \frac{\alpha}{\mathcal{V}_m} \sum_{\Upsilon_{mn} \cap \mathcal{V}_m} \frac{(\phi_n^t - \phi_m^t)}{l_{mn}} t_{mn}^1 C_{mn}^1 = \mathcal{D}_m \tag{3.24}$$

As noted previously, three methods will be used by which to calculate $\mathcal{D}_m$ viz. upwinding, a characteristic based method and artificial dissipation. These are detailed next.

3.4.1.1 First-order Accurate Stabilisation: Upwinding

The above discretisation scheme may be stabilised through the addition of standard upwinding, but at the cost of degenerating the spatial accuracy to first order. This method is however considered of value for the purpose of validating the improvement in accuracy resulting from the other high-resolution schemes.

The upwinding term $\mathcal{D}_m$ is calculated as:

$$\mathcal{D}_m = \sum_{\Upsilon_{mn} \cap \mathcal{V}_m} \frac{|u_1|}{2} \left(\phi_n^t - \phi_m^t\right) t_{mn}^1 C_{mn}^1 \tag{3.25}$$

where the nomenclature is as defined previously.

3.4.1.2 Higher-order Accurate Stabilisation: Characteristic Based Method

As noted above, the addition of upwinding destroys the natural notionally second-order spatial accuracy of the outlined edge-based finite volume scheme. This may, however, be preserved through the use of a more advanced stabilising operator.

[1] Courant-Friedrichs-Lewy number.

One such method is the Lax-Wendroff type method[1] (Kallinderis [35], Zienkiewicz & Taylor [81]). This characteristic based technique has recently shown promise in stabilising incompressible flow systems involving single-phase flow (Zienkiewicz & Codina [80]) as well as flow through porous domains (Massarotti *et al.* [48]).

An outline of how this method was constructed in the context of the one-dimensional advection-diffusion equation is given in Appendix B. The final discreet expression which results for the stabilizing term $\mathcal{D}_m$, is as follows:

$$\mathcal{D}_m = \frac{\Delta t_{conv}}{2CFL\mathcal{V}_m} u_1^2 \sum_{\Upsilon_{mn} \cap \mathcal{V}_m} \frac{(\phi_n^t - \phi_m^t)}{l_{mn}} t_{mn}^1 C_{mn}^1 \tag{3.26}$$

where the nomenclature is as defined previously and $\Delta t_{conv} = \Delta x_1 / u_1$.

3.4.1.3 Higher-order Accurate Stabilisation: Artificial Dissipation

The third method evaluated for the purpose of the stabilisation evaluation exercise, is the so-called JST method (Jameson, Schmidt, Turkel) as proposed by Jameson *et al.* [34]. This method involves the addition of a biharmonic operator to the RHS of Equation (3.19) and is shown to offer accurate solutions by the aforementioned authors.

The stabilizing term $\mathcal{D}_m$ is now calculated in an edge-based manner as per Mavriplis [49], from which the following results:

$$\mathcal{D}_m = 2u_1 \mathcal{V}_m^2 \varepsilon_4 \sum_{\Upsilon_{mn} \cap \mathcal{V}_m} \left[\sum_{\Upsilon_{mn} \cap \mathcal{V}_m} \left(\phi_m^t - \phi_n^t \right) \right] \tag{3.27}$$

where ε_4 is an empirical constant, the value of which is to be determined through numerical experimentation, and such that the smallest value which eliminates spurious oscillations, is chosen.

3.4.1.4 Stabilisation Evaluation Results and Conclusion

The one-dimensional model problem will now be solved with the three stabilisation methods. The results are presented for three different Peclet numbers viz. $\mathrm{Pe} = \{2, 10, 50\}$, using five elements. The aforementioned Peclet number range

[1] Termed *Characteristic Based* (CB) in the context of finite element methods.

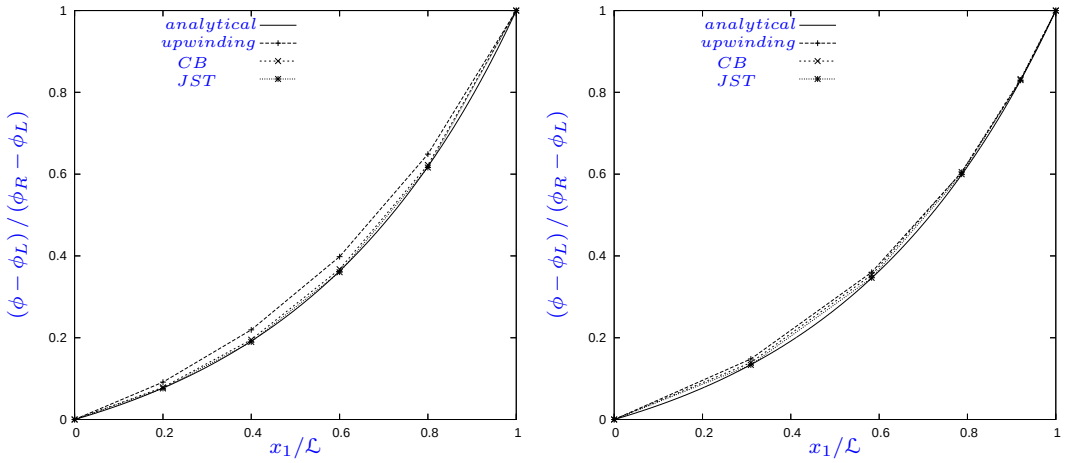

Figure 3.2: Predicted solution to the advection-diffusion equation compared to the analytical solution for a Peclet number of 2. Predictions as obtained on an equal-spaced (left) and preferentially stretched (right) mesh containing five elements are shown. CB and JST denote the *characteristic based* and *artificial dissipation* stabilisation schemes respectively. The subscripts L and R indicate the left and right boundaries respectively.

and number of elements were chosen to coincide with that presented by Bathe [4]. Four curves are presented per graph, one being the analytical solution and the remaining three indicate the solution obtained with each of the three stabilisation schemes as presented in the preceding text. Note that the tests are done for both equal-spaced and preferentially stretched meshes.

Figure 3.2 shows that for low Peclet numbers, the solutions obtained with both upwinding- and the high resolution stabilization schemes show no pronounced deviation from the analytical solution. At moderate and high Peclet numbers though, substantial deviations are distinguishable on both the stretched and equal-spaced meshes (Figures 3.3 and 3.4). Upwinding is seen to be less accurate than the high-resolution schemes, with artificial dissipation rendering the better solution on the stretched meshes. On the equal-spaced meshes at moderate and high Peclet numbers, artificial dissipation displays unstable behavior (Figures 3.3 and 3.4), whereas the characteristic based method, although not as accurate as artificial dissipation, appears more stable.

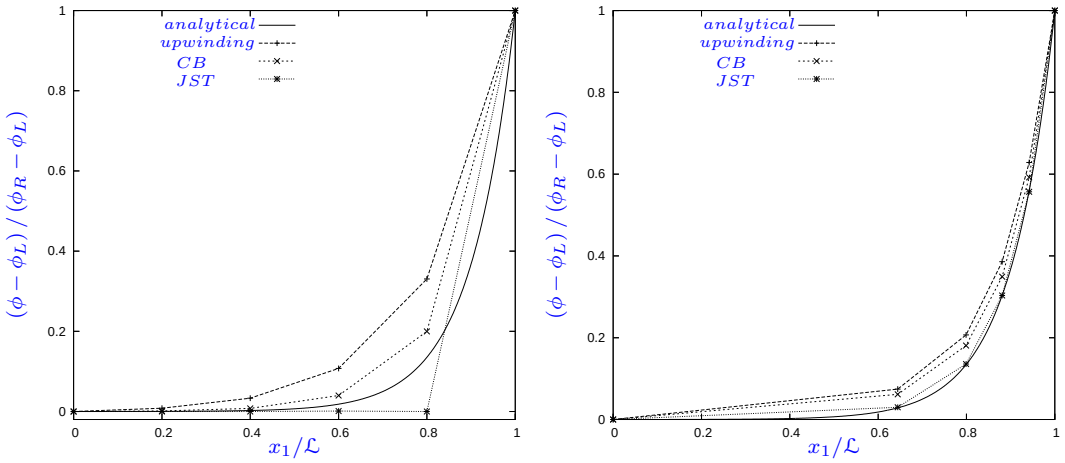

Figure 3.3: Predicted solution to the advection-diffusion equation compared to the analytical solution for a Peclet number of 10. Predictions as obtained on an equal-spaced (left) and preferentially stretched (right) mesh containing five elements are shown.

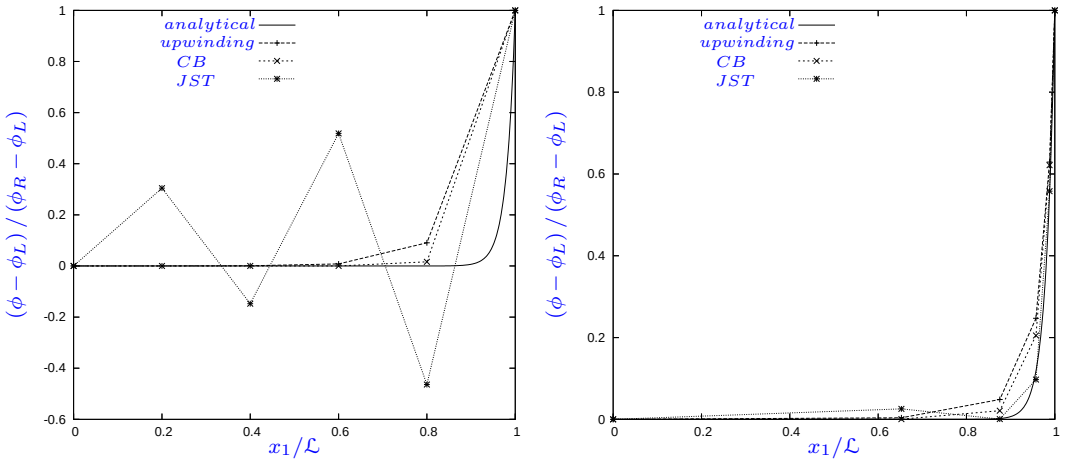

Figure 3.4: Predicted solution to the advection-diffusion equation compared to the analytical solution for a Peclet number of 50. Predictions as obtained on an equal-spaced (left) and preferentially stretched (right) mesh are shown.

Considering the results of the above numerical study, the following conclusions can be drawn:

- The upwinding stabilization scheme reduces the order of accuracy of the solution. This is the case especially at appreciable Peclet numbers.
- Stretching of the mesh to increase the cell density in the region of high gradients improves the solution obtained. Note that for the high Peclet numbers the stretching ratio exceeds two.
- An empirical constant $\varepsilon_4 = 0.001$ was used for the artificial dissipation method. At higher Peclet numbers, this method is seen to produce oscillations if the mesh spacing is not representative of the gradients in the flow field, whereas the characteristic based method appeared more stable.
- The solutions as obtained with the two higher-order methods are seen to be very similar on stretched meshes, with artificial dissipation the more accurate method.

In view of the above, it is concluded that the characteristic based method proved more robust and simpler to apply since there is no empirical constant to tune. Artificial dissipation proved more accurate on stretched meshes. As the latter is the case in this work, artificial dissipation was the method chosen for stabilisation, and is detailed next.

3.4.2 Artificial Dissipation

In the context of the governing equations under consideration, the JST scheme of Jameson *et al.* [34] involves the addition of an artificial dissipation term to the right-hand side of the discretized governing equation (Equation (3.18)). The dissipation term $\mathbf{D}$ is again constructed in an edge-based manner as per Mavriplis [49]:

$$\boldsymbol{D}_m = -\varepsilon_4 \frac{\Lambda_m + \Lambda_n}{2} \sum_{\Upsilon_{mn} \cap \mathcal{V}_m} \left(\nabla^2 \boldsymbol{W}_n^{ad} - \nabla^2 \boldsymbol{W}_m^{ad} \right) \tag{3.28}$$

where $\boldsymbol{W}$ is the compressible primitive variable vector and the superscript ad refers to the artificial dissipation implementation of the first harmonic operator. The relation employed for the latter in this work is based on that proposed by Malan *et al.* [46], but extended/generalised to account for the heterogeneous nature of the continuum under consideration as follows:

$$\nabla^2 \boldsymbol{W}_m^{ad} = \sum_{\Upsilon_{mn} \cap \mathcal{V}_m} \left. \frac{\partial \boldsymbol{W}}{\partial \boldsymbol{Q}^{ad}} \right|_{\overline{f}_{mn}} \left(\boldsymbol{Q}_n^{ad} - \boldsymbol{Q}_m^{ad} \right) \tag{3.29}$$

where

$$\left. \frac{\partial \boldsymbol{W}}{\partial \boldsymbol{Q}^{ad}} \right|_{\overline{f}_{mn}} = \begin{pmatrix} \left. \overline{r\varepsilon / c_{\tau cont-mom}^2} \right|_{mn} & 0 & 0 & 0 \\ \left. \overline{r\varepsilon \left\langle u_1 \right\rangle^f / c_{\tau cont-mom}^2} \right|_{mn} & \overline{\left\langle \rho_f \right\rangle^f}_{mn} & 0 & 0 \\ \left. \overline{r\varepsilon \left\langle u_2 \right\rangle^f / c_{\tau cont-mom}^2} \right|_{mn} & 0 & \overline{\left\langle \rho_f \right\rangle^f}_{mn} & 0 \\ \left. \overline{r\varepsilon \left\langle C_{p_f} \right\rangle^f / c_{\tau cont-mom}^2} \right|_{mn} & 0 & 0 & \overline{\left\langle \rho_f \right\rangle^f}_{mn} \left\langle C_{p_f} \right\rangle^f \end{pmatrix} \tag{3.30}$$

and

$$\boldsymbol{Q}^{ad} = \begin{pmatrix} \left\langle p \right\rangle^f \\ r\varepsilon \left\langle u_1 \right\rangle^f \\ r\varepsilon \left\langle u_2 \right\rangle^f \\ r\varepsilon \left\langle T_f \right\rangle^f \end{pmatrix} \tag{3.31}$$

Here $\left. \overline{\bullet} \right|_{mn}$ again denotes the edge-averaged quantities.

The scaling coefficient vector Λ similarly requires generalisation to address the large disparity in eigenvalues between the fluid energy and momentum conservation equations. For this purpose, the following vector relation is employed in this work:

$$\Lambda_m^j = \sum_{\Upsilon_{mn} \cap \mathcal{V}_m} \left| \left\langle \boldsymbol{u} \right\rangle^f \cdot \boldsymbol{C}_{mn} \right| + \left(c_{\tau cont-mom} \left(1 - \delta_{4j} \right) + c_{\tau enerf} \delta_{4j} \right) \left| \boldsymbol{C}_{mn} \right| \tag{3.32}$$

where $c_{\tau enerf}$ denotes the maximum velocity of information propagation seen by the fluid energy equation, which is calculated as:

$$c_{\tau enerf} = \frac{\left\langle k_f \right\rangle^f}{\left\langle \rho_f \right\rangle^f \left\langle C_{p_f} \right\rangle^f \Delta\chi\sigma_{vn}} + \left| \left\langle \boldsymbol{u} \right\rangle^f \right| \tag{3.33}$$

where it is typical to set $\sigma_{vn} = 0.5$. Note that the scaling coefficients are never a function of radius or porosity, which is consistent with the fact that the latter should in no way influence the velocity of information propagation.

3.5 Temporal Discretisation

Temporal discretisation is achieved via a forward difference methodology. As a steady-state solution is sought, the largest allowable appropriate time-step size is employed for each governing equation resulting in the following fully discrete equation at a node m:

$$\left[\begin{array}{c} 1/\Delta t_{\tau_{cont-mom}} \\ 1/\Delta t_{\tau_{cont-mom}} \\ 1/\Delta t_{\tau_{cont-mom}} \\ 1/\Delta t_{\tau_{enerf}} \\ 1/\Delta t_{\tau_{eners}} \end{array}\right]\Bigg|_m \boldsymbol{I}\,\frac{\partial \boldsymbol{W}}{\partial \boldsymbol{Q}}\Bigg|_{\overline{g}_m}^{t_\tau}\left(\boldsymbol{Q}_{\overline{g}_m}^{t_\tau+\Delta t_\tau} - \boldsymbol{Q}_{\overline{g}_m}^{t_\tau}\right) = \boldsymbol{RHS}_m \tag{3.34}$$

where $\boldsymbol{I}$ and $\boldsymbol{RHS}$ respectively are the identity matrix and spatially discretised terms placed on the right-hand-side. Further, the subscripts $cont{-}mom$, $enerf$ and $eners$ respectively denote the values pertaining to the continuity and momentum, fluid energy and solid energy equations. The largest allowable time-step is employed per cell, i.e. local-time-stepping, and is calculated for each equation as:

$$\Delta t_{\tau_\zeta} = \frac{CFL\Delta\chi}{\lambda_\zeta} \tag{3.35}$$

where the subscript ζ is the specific equation type ($cont - mom$, etc.) and λ is an approximation of the maximum eigenvalue associated with each. The latter is calculated in a manner which is consistent with the preconditioned equations as follows:

$$\begin{aligned}
\lambda_{cont-mom} &= \frac{1}{2}\left((2-a_u)\left|\langle \boldsymbol{u}\rangle^f\right| + \sqrt{\left|\langle \boldsymbol{u}\rangle^f\right|\left|\langle \boldsymbol{u}\rangle^f\right|(2-a_u)^2 + 4c^2_{\tau_{cont-mom}}}\right) \\
\lambda_{enerf} &= c_{\tau enerf} \\
\lambda_{eners} &= \frac{k_{eff}}{\langle \rho_s\rangle^s \langle C_{p_s}\rangle^s (1-\varepsilon)\Delta\chi\sigma_{vn}}
\end{aligned} \tag{3.36}$$

where the effective thermal conductivity is divided by the relevant porosity function to return the intrinsic value.

3.6 Conclusion

In this chapter, the numerical solution procedure was discussed. The aforementioned involves the spatial and temporal discretisation strategies, stabilisation technique, and a method of addressing the numerical stiffness of the system as a result of fluid incompressibility. The latter was overcome by applying the method of artificial compressibility, while artificial dissipation was chosen to stabilise the numerical system.

Chapter 4

Numerical Tests and Validation

4.1 Introduction

The developed modelling technology is evaluated in terms of both stability and accuracy via the solution of three problems. As largely varying porosity (heterogeneous porous material) is a focus of this work, the test cases are selected to serve as a stringent test for the developed related modelling technology as follows:

- Flow through a channel with varying porosity (Section 4.2).
- Natural convective flow in the SANA test facility [51]: 5 kW and 35 kW cases (Section 4.3). Both constant and varying porosity mathematical descriptions are considered in order to quantify the influence of accounting for porosity variation on modelling accuracy. Note further that the aforementioned two test cases were selected as these represent the two extreme SANA tests in terms of total heating input.

In all cases, accuracy is assessed by comparison of predicted results with analytical or experimental data. A further comparison of the predicted results for the SANA test cases is made with numerical results published by du Toit *et al.* [15], as obtained using a systems CFD code. Similar boundary conditions are accounted for in both models, but the results shown are subject to different methods of application of these. As a result of the aforementioned difference, a rigorous comparison was not possible and the results are assigned to Appendix C.

4.2 Porous Channel Flow

The first test case involves incompressible, isothermal flow through a channel with varying porosity. Note that for the purpose of serving as a stringent test for the developed stabilisation methodology, the only viscous effects considered were those due to solid matrix drag, i.e. a purely convective system with comparatively small source term results. A schematic diagram of the channel with arbitrary unstructured mesh is shown in Figure 4.1, with the chosen porosity variation being depicted in Figure 4.2. Note the large porosity variation in terms of both magnitude and gradient.

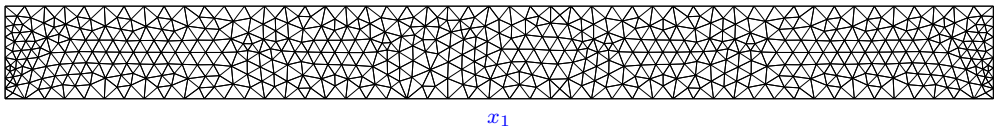

Figure 4.1: Porous channel mesh.

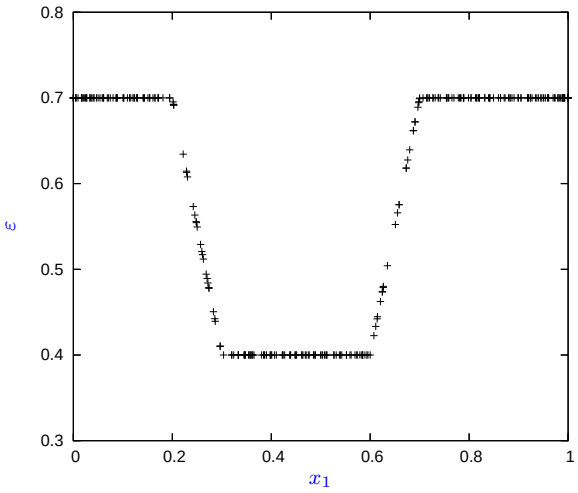

Figure 4.2: Channel porosity distribution.

The boundary conditions applied are as follows:

- A velocity and pressure inflow boundary is prescribed.

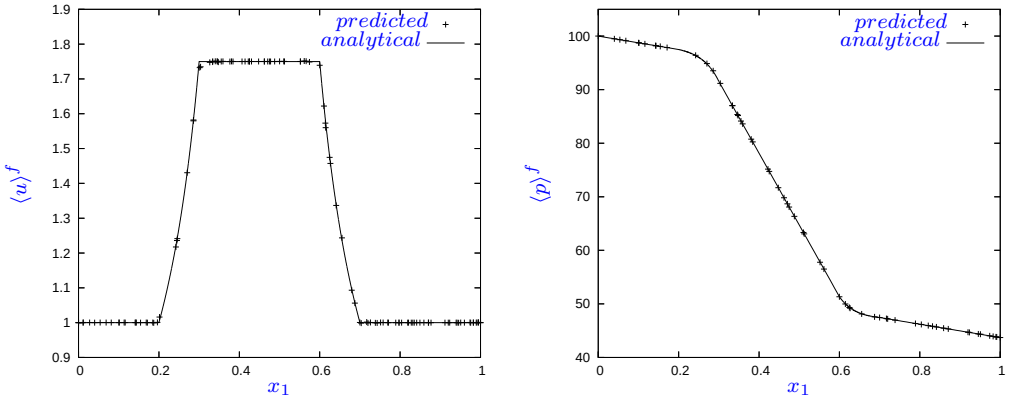

Figure 4.3: Porous channel velocity (left) and static pressure (right) distribution.

- The velocity prescribed at the outflow boundary is identical to the inflow, as the flow area is the same.
- Slip boundary conditions are applied to the top and bottom walls.

An analytical solution to $\langle \mathbf{u}(x_1) \rangle^f$ may be obtained via simple mass conservation. Further, $\langle p(x_1) \rangle^f$ may be obtained via the solution of the one-dimensional Bernoulli equation with drag term. These are shown, together with the values predicted by the developed solver, in Figure 4.3. From the figure, it is clear that the aforementioned compare well, validating the efficiency of the developed technology to model the convective flow component in highly heterogeneous materials.

4.3 SANA Test Set-up

The developed numerical technology is validated next by application to a benchmark problem, viz. the SANA test set-up at the Jülich Research Centre [51]. The set-up, which is shown schematically in Figure 4.4, consists of an annular cylindrical vessel with internal diameter of 1.5 m and height of 1 m. The vessel is filled with 60 mm randomly packed graphite spheres. The working fluid considered in this work is helium (pressurised to 1 bar). The heat input to the system is via a centrally placed electrical heater. The top and bottom of the vessel are

insulated while heat is allowed to escape from the outer annular surface. The following two operating conditions were selected for the purpose of validation:

- Steady-state test with heating element spanning the full length of the pebble bed, with 5 kW nominal heating power input.
- Similar operating conditions to the aforementioned, with the exception of a heating power input increase to 35 kW.

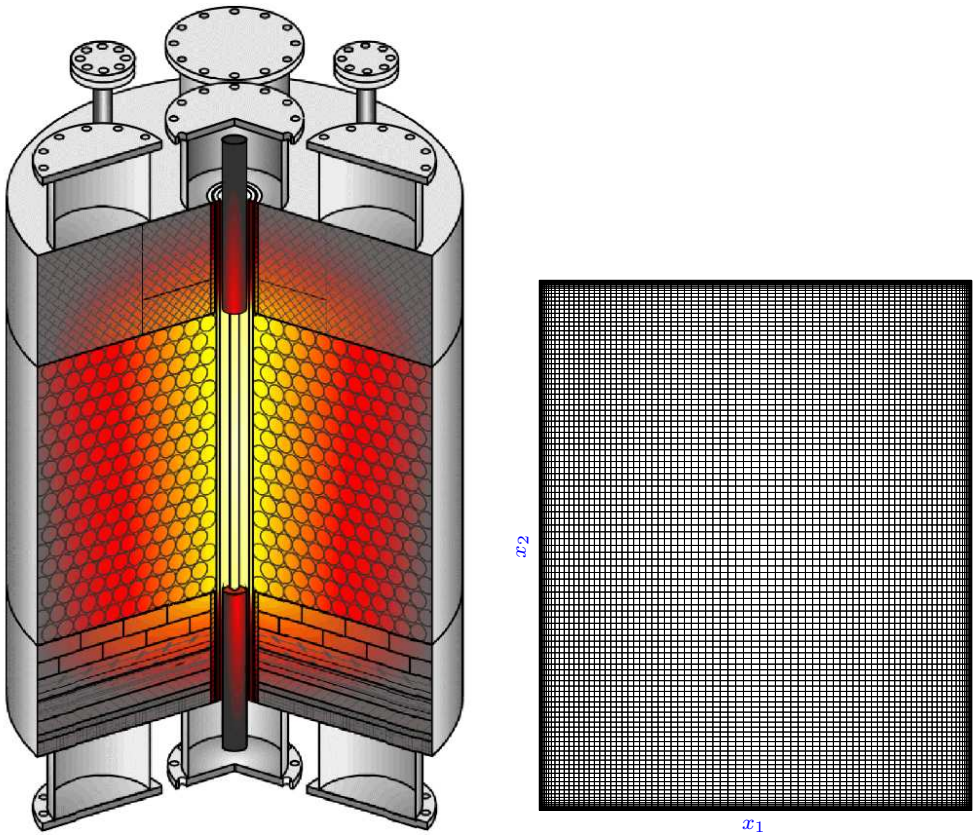

Figure 4.4: Schematic diagram of the SANA test set-up (left) with central heating element taken from [51] and the representative axisymmetric mesh used (right).

The heat-transfer processes to be modelled are the influx of heat from the inner wall to both the working fluid and solid pebbles, conduction and radiative heat transfer within the solid phase, convective heat transfer between the solid

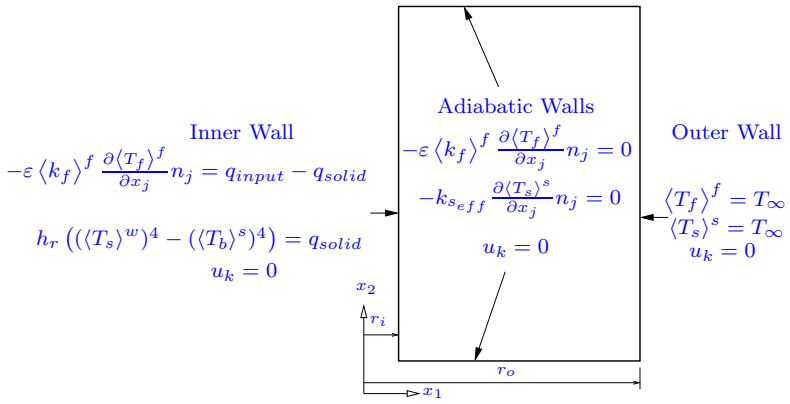

Figure 4.5: Schematic diagram of the geometry and boundary conditions applied. Here, r_i and r_o denote the internal and external radii respectively and q_{input} and q_{solid} the respective heat fluxes as calculated using Equations (2.28) and (2.31).

and fluid phase, whilst conduction and convective heat transfer are the modes of heat transfer within the fluid phase. As a result of buoyancy forces, a convection current develops with upward movement near the hot inner wall and downward movement near the colder outside wall. The top and bottom walls are insulated.

The above was simulated via a two-dimensional axisymmetric model to which the following boundary conditions and porosity variation were applied (see Figures 4.5 and 4.6):

- No-slip boundary conditions are applied to all the walls.
- The top and bottom walls are treated as adiabatic.
- Constant uniform heat flux is applied to the inner wall.
- A constant temperature field is applied to the outer wall (temperatures applied were taken from the experimental measurements).
- Porosity is allowed to vary between 0.39 and 0.99 as per Equations (2.11) and (2.12) for the heterogeneous test cases, while the porosity is fixed at 0.39 for the constant porosity cases.

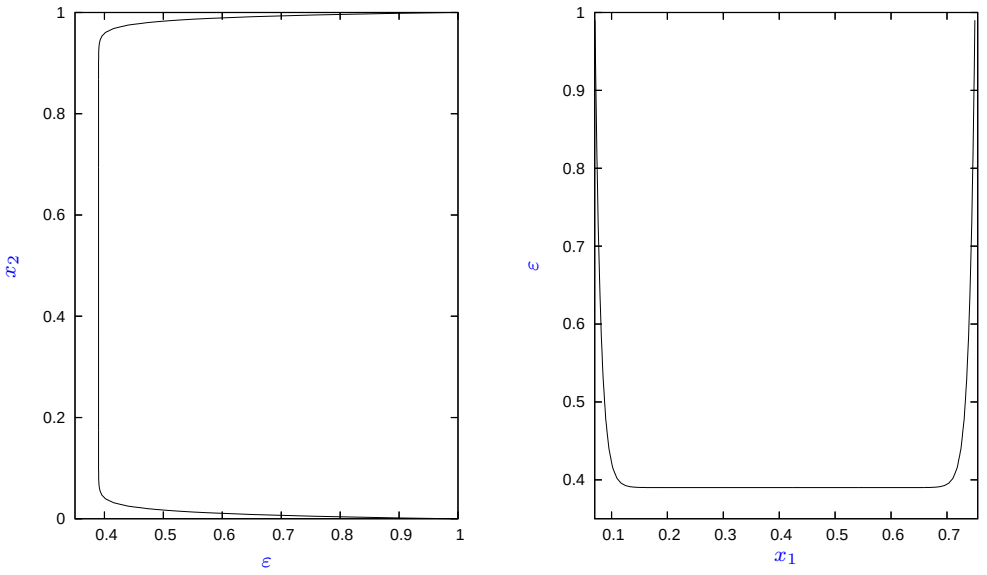

Figure 4.6: Porosity distribution at the horizontal (left) and vertical (right) centrelines, as applied to the variable porosity SANA test cases.

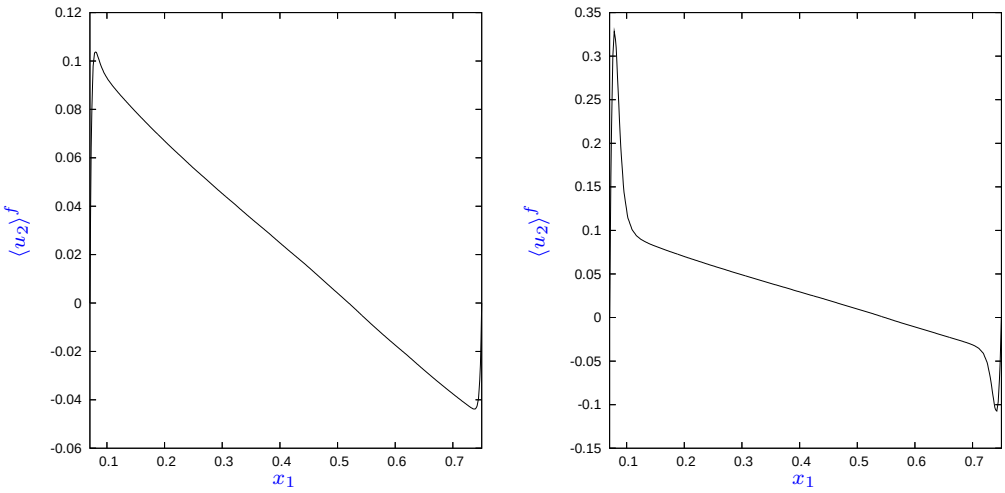

Figure 4.7: Vertical velocities in radial section at 0.5 m vertical elevation for constant and variable porosity 5 kW test cases.

The mesh for both the 5 kW and 35 kW test cases is shown in Figure 4.4. The structured mesh contains 9 296 elements with local refinement near the walls

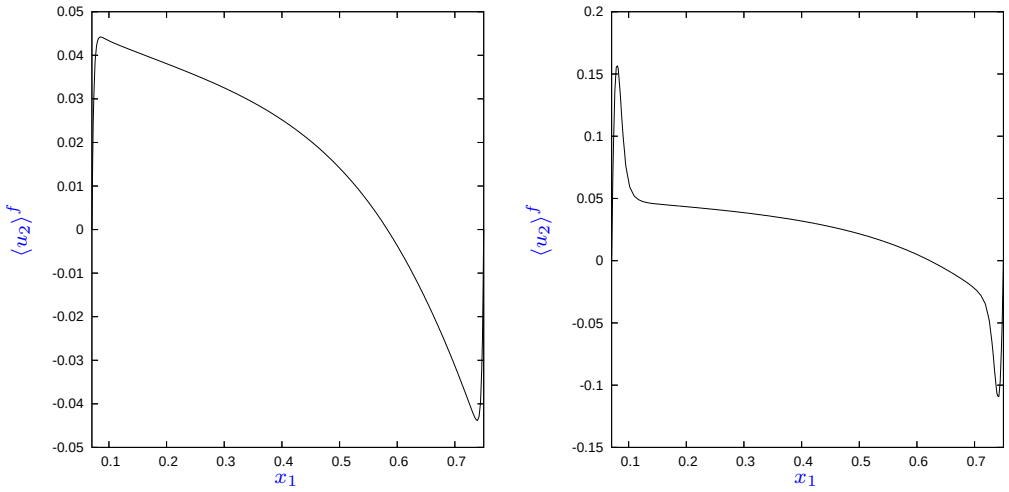

Figure 4.8: Vertical velocities in radial section at 0.5 m vertical elevation for constant and variable porosity 35 kW test cases.

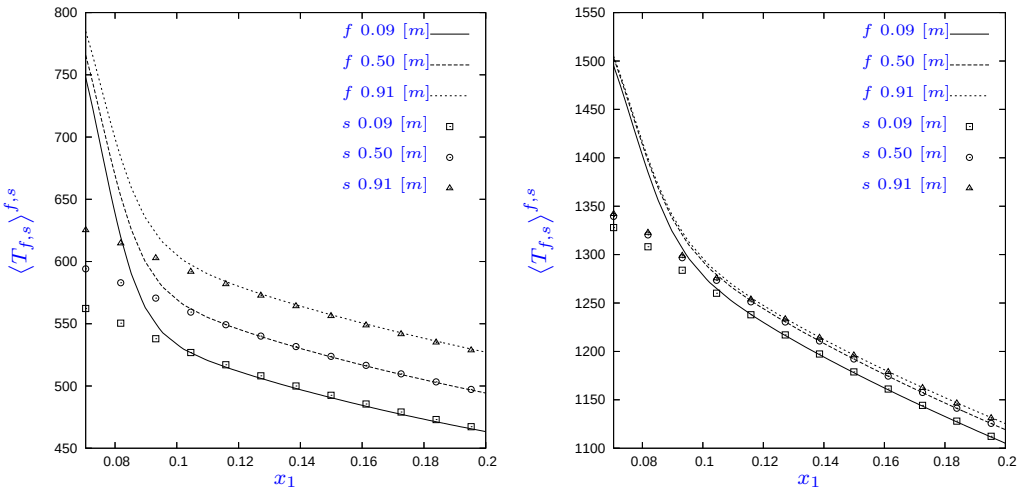

Figure 4.9: Predicted temperature distribution of the solid (s) and fluid (f) phases at the inner wall for the variable porosity 5 kW (left) and 35 kW (right) test cases.

to capture the larger gradients in temperature and velocity expected in these regions. For this purpose, the near-wall region contains ten (10) data points with minimum cell size normal to the boundary being 1 mm in size (1/60 th of a pebble diameter).

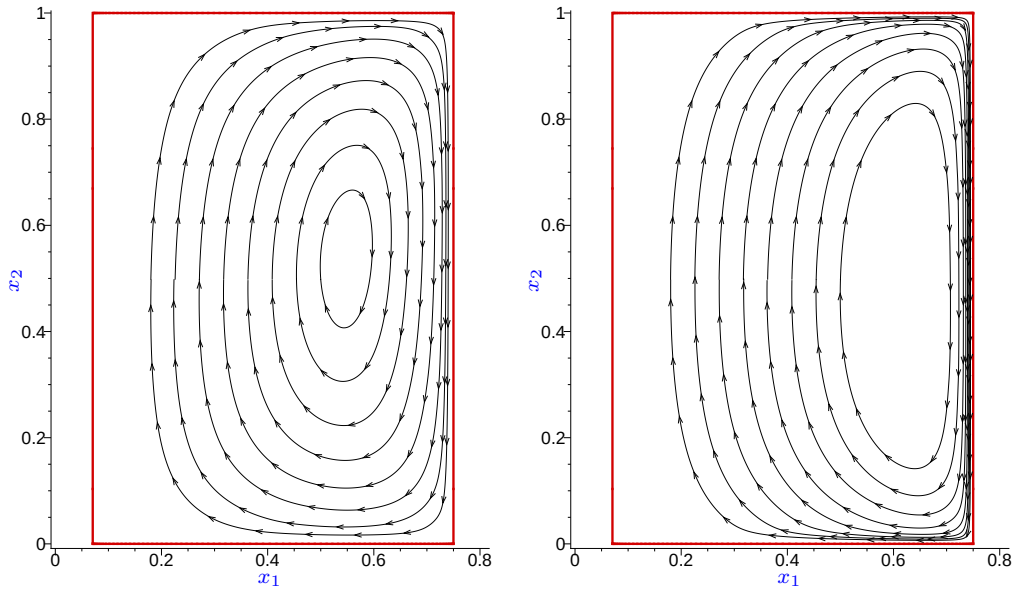

Figure 4.10: Streamlines for the variable porosity 5 kW (left) and 35 kW (right) cases.

The calculated velocities at a section through the vertical centreline of the packed bed are shown in Figures 4.7 and 4.8 for both the constant (homogeneous) and varying porosity (heterogeneous) cases. The overall velocity profiles are seen to differ markedly for the respective cases. To explain this, reference is made to the porosity distribution as given in Figure 4.6. The velocity peaks of the varying porosity cases are seen to be substantially higher than their constant porosity counterparts, which is a direct consequence of the decreased solid matrix drag due to the porosity increase as the solid boundary is approached (Figure 4.6). A further consequence of the heterogeneous approach can clearly be seen in the prediction of the wall-channelling effect, where sharp velocity peaks are seen close to the solid boundaries corresponding to areas of increased porosity (the pronounced channelling effect is not observed for the homogeneous case). This wall-channelling effect has been observed experimentally by several authors (Benenati & Brosilow [7],White & Tien [76]), and claimed to significantly influence local heat transfer characteristics (Prasad *et al.* [56], Vafai *et al.* [69]). It may be further noted from the figures, that the maximum velocity is predicted

to occur within half a sphere diameter of the wall for the heterogeneous cases, which is similarly consistent with experimental measurements from the literature (Price [57], Giese *et al.* [25]). A further observation from Figures 4.7 and 4.8 is the fact that the velocity peak for both the constant and variable porosity 35 kW cases are lower than predicted for the 5 kW cases. This is due to the fluid phase temperatures of the 35 kW case being substantially higher than the 5 kW case (see Figure 4.9), resulting in a significant increase in viscosity of the helium. It is further noted that although the overall velocity profiles differ markedly between the constant and variable porosity cases, the velocity distributions in the homogeneous sections of the respective cases show similar trends. Figure 4.9 further shows the large disparity between the predicted solid- and fluid phase temperatures close to the heated inner wall. Capturing this accurately is essential for the correct prediction of the fluid temperature, which is in turn necessary for the correct application of the radiative boundary condition (Equation (2.28)). Figure 4.10 shows streamlines which depict the natural convection currents present inside the vessel. The velocity distributions are non-symmetrical as a result of the axi-symmetric geometry as well as the strong temperature dependence of the material properties.

The predicted pebble temperature distributions at three different heights are compared to measurements in Figure 4.11. The resulting normalised deviation between measured and predicted values is depicted in Figure 4.12. The said normalised temperature deviation is calculated as:

$$\Delta \langle T_s \rangle^s_{normalised} = \frac{\left| \langle T_s \rangle^s_{predicted} - \langle T_s \rangle^s_{measured} \right|}{\langle T_s \rangle^s_{max} - \langle T_s \rangle^s_{min}} \tag{4.1}$$

where $\langle T_s \rangle^s_{max}$ and $\langle T_s \rangle^s_{min}$ are respectively the maximum and minimum measured temperatures. What is clear from the comparison is that commendable modelling accuracy was achieved, with the maximum and average errors being 0.18 and 0.034 for the constant porosity, and 0.12 and 0.03 for the variable porosity cases respectively. The quoted maximum errors highlight a significant and important improvement in accuracy, on account of porosity variation being fully accounted for.

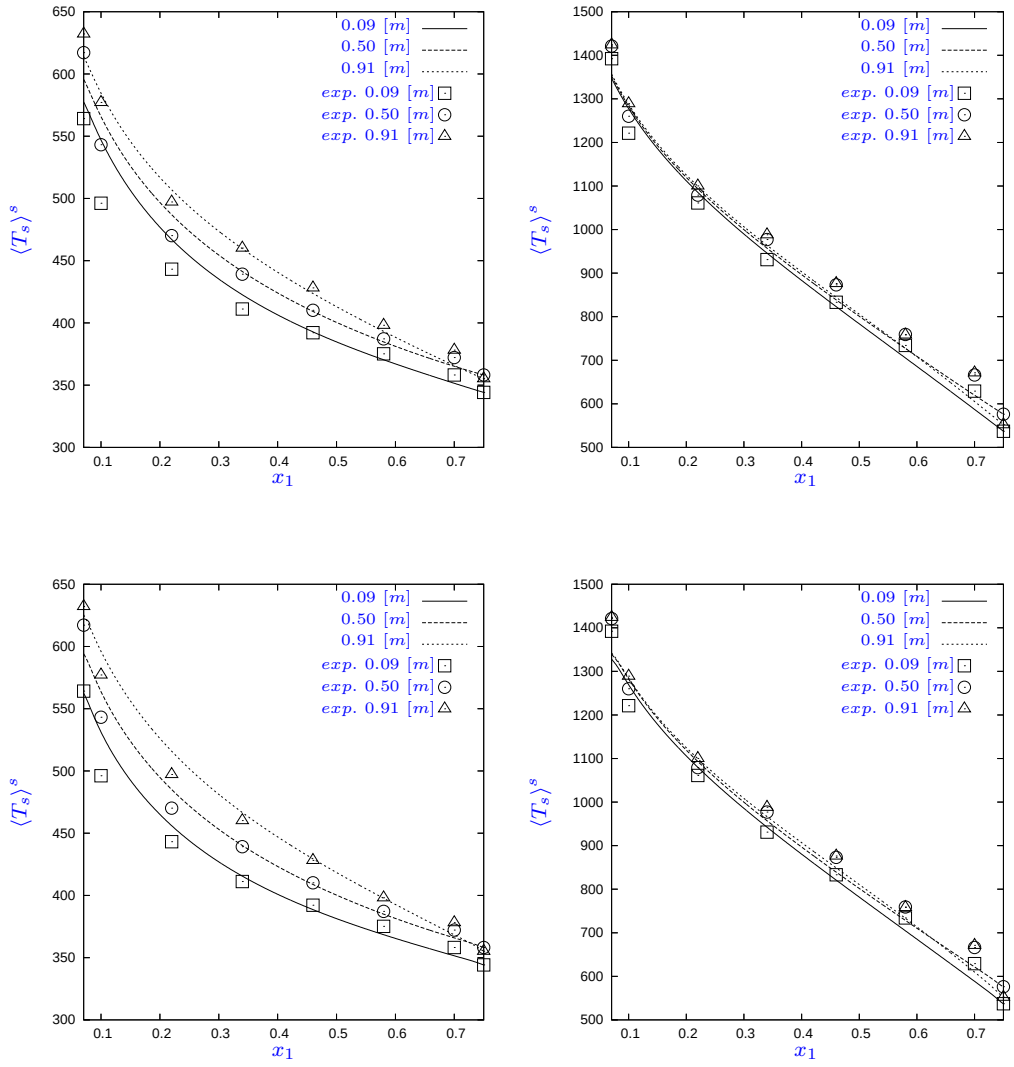

Figure 4.11: Predicted pebble temperature distribution compared to experimental (exp.) measurements for the 5 kW (left) and 35 kW (right) cases. The comparisons are done at three different heights. The top figures detail the constant porosity test cases, and the bottom figures the variable porosity test cases.

Following from the commendable agreement between measured and predicted data, the Neumann radiative-type boundary condition from the model of Schlünder applied to the inner wall (Equations (2.28) and (2.31)), critical to the correct specification of heat influx to the respective phases, proved sound. Furthermore,

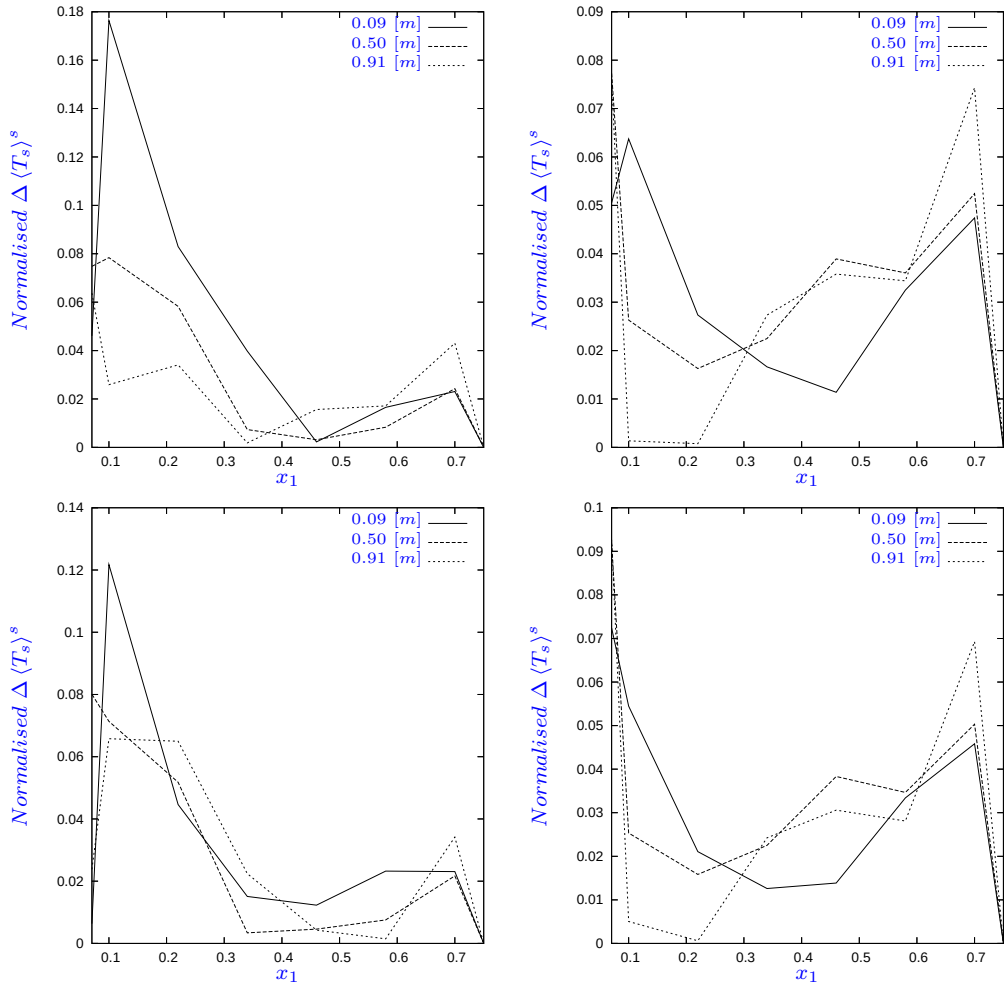

Figure 4.12: Normalised temperature disparity between predicted and measured solid-phase temperatures for the 5 kW (left) and 35 kW (right) cases. The top figures detail the constant porosity test cases, and the bottom figures the variable porosity test cases.

the agreement between the slope of the predicted temperature distribution and experimental data indicates that the effective thermal conductivity is calculated to within acceptable limits.

Finally, the solution process residual plots for the respective test cases are given in Figures 4.13 and 4.14. Here, the residual is calculated as the average Euclidean norm of all five conservation equations solved for. The monotone drop

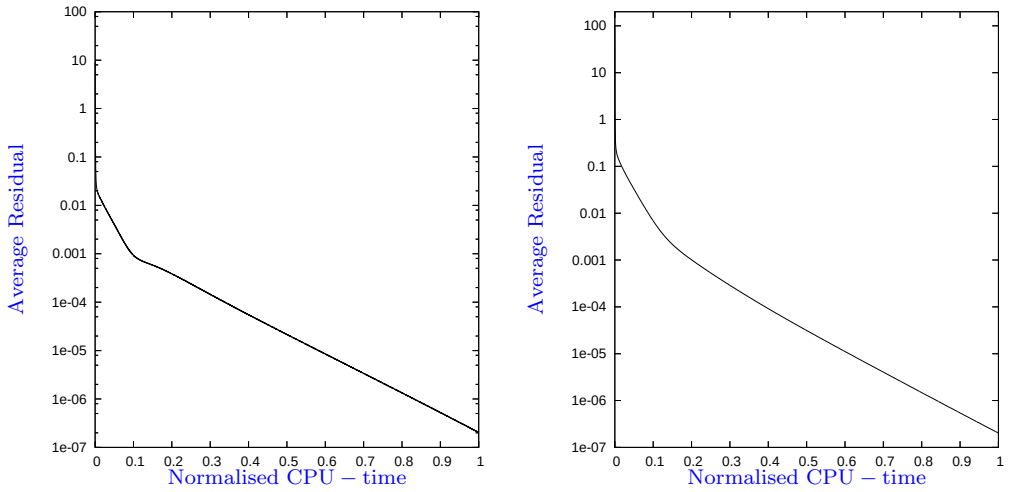

Figure 4.13: Average residual for the constant porosity 5 kW (left) and 35 kW (right) cases.

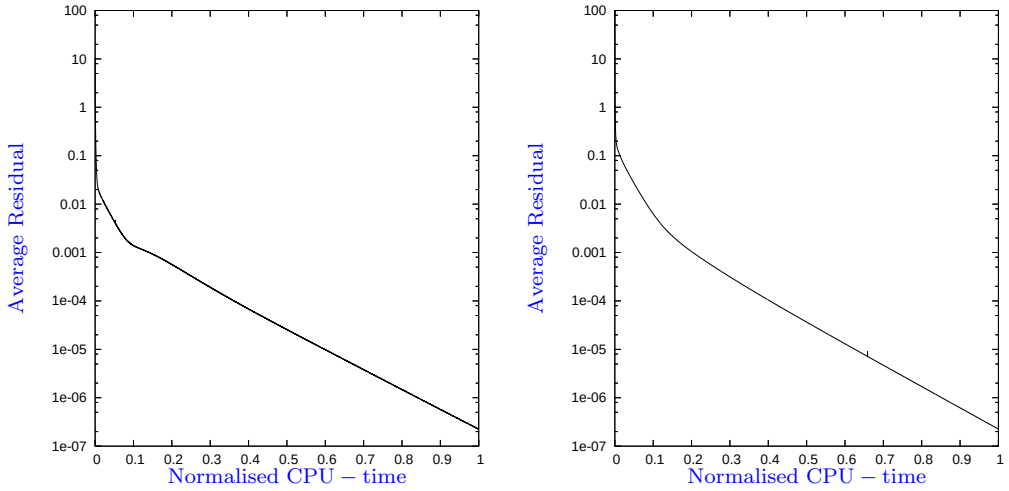

Figure 4.14: Average residual for the variable porosity 5 kW (left) and 35 kW (right) cases.

in residual is indicative of a stable solution process. The simulations were run on a personal computer with a 3 *GHz Intel Pentium* 4 processor and 2 Gigabytes memory, taking on average 239 hours and 1.9 million iterations to complete. The reason for the excessive simulation times is the allowable time step size being a

function of $\Delta\chi^{-2}$ (refer to Equations (3.35) and (3.36)) because of the explicit solution procedure. The refined mesh used in the near-wall region, able to capture local gradients, therefore causes a quadratic reduction in the allowable time step size.

4.4 Conclusion

This chapter detailed the comparisons between predicted, analytical and experimental results for the purpose of validating the developed numerical modelling technology. Comparisons were done for three test cases, viz. a varying porosity channel and the SANA 5 kW and 35 kW cases. Both constant and varying porosity analyses of the SANA cases were conducted and commendable accuracy achieved. The importance of properly accounting for porosity variation, as well as local thermal disequilibrium, to solution accuracy was demonstrated. This is as the aforementioned allowed for the modelling of phenomena such as wall-channelling and pebble-wall heat transfer.

Chapter 5

Conclusion and Recommendations

5.1 Conclusion

This work was concerned with the modelling of heat and mass transfer within buoyancy-driven flow through saturated packed pebble-beds. A generalised volume-averaged partial differential governing equation set was employed, and such that local thermal disequilibrium between the two phases considered, viz. fluid and solid, was accounted for. The governing equation set was written such that both two-dimensional and axisymmetric formulations are possible, and a void fraction variation of 0.39 to 0.99 allowed for. The latter was done in order to allow explicit modelling of phenomena such as wall-channelling and wall-bed radiative heat transfer.

Material properties were taken as fully non-linear with respect to temperature, and the resulting set of coupled non-linear partial differential equations solved via a locally preconditioned artificial compressibility method. Spatial discretisation was effected with a compact finite volume edge-based discretisation method. In the interest of accuracy, stabilisation was effected via the JST scalar-valued artificial dissipation method.

The developed technology was successfully validated by application to the modelling of a channel flow test case as well as the SANA benchmark experimental setup. The channel flow test case confirmed the suitability of the chosen

numerical solution method at resolving convective flow through highly heterogeneous materials. The SANA test cases confirmed the ability of the developed modelling technology to accurately model complex heat and fluid flow phenomena in real engineering devices. A minimum mesh spacing of $1/60\ th$ of a pebble diameter and ten data points in the near wall region was used to prescribe the heterogeneous porous field and resolve the resulting near-wall flow and heat transfer phenomena. As a result, flow features such as wall channeling were successfully predicted, and predicted temperatures shown to compare well with measured data in all cases. The maximum and average normalized temperature deviation was 0.18 and 0.034 for the homogeneous, and 0.12 and 0.03 for the heterogeneous cases respectively. Properly accounting for variable porosity as well as local thermal disequilibrium was therefore shown to be of significant importance.

5.2 Recommendations and Future Work

The following recommendations naturally follow from the shortcomings highlighted in the foregoing text, as well as from an ongoing endeavour to have numerical modelling represent nature:

- The directional invariance of the current empirically derived constitutive equations and the subsequent accuracy of continuum based numerical predictions employing these relations are to be investigated.

- Empirical models used (Constitutive Equations (Section 2.3)) to account for the microscopic behaviour are necessarily restricted to a valid range of applicability based on specified parameters related to the physical set-up. Details on exactly how these correlations were generated and their applicability are not necessarily available or clear from the literature. Experimental work, furthering the available data published mainly in the 1950′s and 60′s, is therefore crucial if a continuum volume-averaged approach to modelling flow and heat transfer through porous media is to be meaningfully pursued.

- Allowing for the explicit modelling of porosity variation did improve the predicted results, yet the overall increase in accuracy is not perceived to be substantial. There are a number of possible factors contributing to this:

  - The chosen SANA test cases (natural convection) are not necessarily ideal for demonstrating the effect of wall-channeling due to a varying porosity field on the overall heat transfer. It is expected that a comparative forced convection test case would be better suited, as the momentum transfer should be greater.
  - The certainty bound for the constitutive equations in the near-wall region is not known, resulting in a possible inaccurate account of the complex microscopic behaviour prevailing in this region at increased flow rates.
  - The diameter ratio of the particle (sphere) to that of the bed is small enough to not have the boundary effects dictate the overall flow phenomena.

  Following from the abovementioned remarks, further sensitivity studies on the different factors influencing the flow phenomena is a just pursuit, given that the validity of all subcomponents are verified as already mentioned.

- Accounting for temperature variation inside a representative pebble is of significant importance when adding neutronics to account for nuclear heat generation. This entails solving for an additional energy equation for the solid phase.

- Conjugate modelling, accounting for container walls, reflector plates, etc. naturally extend the applicability and versatility of the current effort to more realistic physical problems.

- Solution acceleration, using for example multigrid, to speed up the transfer of information in the computational domain and reduce computational time is paramount if sensitivity analysis and design parameter variations are to be done in realistic time.

Appendix A

Material Properties

A.1 Introduction

The material properties as used for the SANA test case (Section 4.3) are given here, viz. that of helium [38] and non-irradiated graphite of type *Sigri AL* 2 − 500 [33, 51]. No reliable source for the specific heat (C_p) of the graphite under consideration was found and the approximate constant value of $1.0e + 003$ was therefore used (Section A.3).

A.2 Material Properties: Helium

Table A.1: Helium Material Properties (pressure = 101.325 kPa).

T $[K]$	ρ $[kg/m^3]$	C_p $[J/kg\ K]$	k $[W/m\ K]$	μ $[kg/m\ s]$
2.930e+002	1.642e-001	5.195e+003	1.515e-001	1.959e-005
3.232e+002	1.489e-001	5.195e+003	1.624e-001	2.098e-005
3.534e+002	1.362e-001	5.195e+003	1.730e-001	2.233e-005
3.836e+002	1.254e-001	5.195e+003	1.834e-001	2.365e-005
4.138e+002	1.163e-001	5.195e+003	1.935e-001	2.494e-005

Continued on next page

T $[K]$	ρ $[kg/m^3]$	C_p $[J/kg\ K]$	k $[W/m\ K]$	μ $[kg/m\ s]$
4.440e+002	1.084e-001	5.195e+003	2.035e-001	2.620e-005
4.742e+002	1.015e-001	5.195e+003	2.132e-001	2.744e-005
5.044e+002	9.541e-002	5.195e+003	2.228e-001	2.865e-005
5.346e+002	9.002e-002	5.195e+003	2.322e-001	2.984e-005
5.648e+002	8.521e-002	5.195e+003	2.414e-001	3.101e-005
5.950e+002	8.089e-002	5.195e+003	2.505e-001	3.216e-005
6.252e+002	7.698e-002	5.195e+003	2.595e-001	3.329e-005
6.554e+002	7.343e-002	5.195e+003	2.683e-001	3.441e-005
6.857e+002	7.020e-002	5.195e+003	2.770e-001	3.552e-005
7.159e+002	6.724e-002	5.195e+003	2.856e-001	3.660e-005
7.461e+002	6.452e-002	5.195e+003	2.941e-001	3.768e-005
7.763e+002	6.201e-002	5.195e+003	3.025e-001	3.874e-005
8.065e+002	5.968e-002	5.195e+003	3.108e-001	3.979e-005
8.367e+002	5.753e-002	5.195e+003	3.191e-001	4.083e-005
8.669e+002	5.553e-002	5.195e+003	3.272e-001	4.185e-005
8.971e+002	5.366e-002	5.195e+003	3.353e-001	4.287e-005
9.273e+002	5.191e-002	5.195e+003	3.432e-001	4.387e-005
9.575e+002	5.027e-002	5.195e+003	3.511e-001	4.487e-005
9.877e+002	4.873e-002	5.195e+003	3.590e-001	4.585e-005
1.018e+003	4.729e-002	5.195e+003	3.667e-001	4.683e-005
1.048e+003	4.593e-002	5.195e+003	3.744e-001	4.780e-005
1.078e+003	4.464e-002	5.195e+003	3.820e-001	4.876e-005
1.109e+003	4.342e-002	5.195e+003	3.896e-001	4.971e-005
1.139e+003	4.227e-002	5.195e+003	3.971e-001	5.066e-005
1.169e+003	4.118e-002	5.195e+003	4.046e-001	5.159e-005
1.199e+003	4.014e-002	5.195e+003	4.120e-001	5.252e-005
1.229e+003	3.916e-002	5.195e+003	4.193e-001	5.344e-005
1.260e+003	3.822e-002	5.195e+003	4.266e-001	5.436e-005
1.290e+003	3.732e-002	5.195e+003	4.338e-001	5.527e-005

Continued on next page

T $[K]$	ρ $[kg/m^3]$	C_p $[J/kg\ K]$	k $[W/m\ K]$	μ $[kg/m\ s]$
1.320e+003	3.647e-002	5.195e+003	4.410e-001	5.617e-005
1.350e+003	3.565e-002	5.195e+003	4.482e-001	5.707e-005
1.380e+003	3.487e-002	5.195e+003	4.553e-001	5.796e-005
1.411e+003	3.413e-002	5.195e+003	4.623e-001	5.885e-005
1.441e+003	3.341e-002	5.195e+003	4.693e-001	5.972e-005
1.471e+003	3.272e-002	5.195e+003	4.763e-001	6.060e-005
1.501e+003	3.207e-002	5.195e+003	4.832e-001	6.147e-005
1.531e+003	3.143e-002	5.195e+003	4.901e-001	6.233e-005
1.562e+003	3.083e-002	5.195e+003	4.969e-001	6.319e-005
1.592e+003	3.024e-002	5.195e+003	5.037e-001	6.404e-005
1.622e+003	2.968e-002	5.195e+003	5.105e-001	6.489e-005
1.652e+003	2.914e-002	5.195e+003	5.172e-001	6.573e-005
1.682e+003	2.861e-002	5.195e+003	5.239e-001	6.657e-005
1.713e+003	2.811e-002	5.195e+003	5.306e-001	6.741e-005
1.743e+003	2.762e-002	5.195e+003	5.372e-001	6.824e-005
1.773e+003	2.715e-002	5.195e+003	5.438e-001	6.906e-005

A.3 Material Properties: Graphite

Table A.2: Sigri AL 2 – 500 Graphite Material Properties.

T $[K]$	ρ $[kg/m^3]$	C_p $[J/kg\ K]$	k $[W/m\ K]$
2.930e+002	1.673e+003	1.000e+003	1.78362e+002
3.232e+002	1.673e+003	1.000e+003	1.67417e+002
3.534e+002	1.673e+003	1.000e+003	1.57285e+002
3.836e+002	1.673e+003	1.000e+003	1.47922e+002
4.138e+002	1.673e+003	1.000e+003	1.39283e+002
4.440e+002	1.673e+003	1.000e+003	1.31325e+002
4.742e+002	1.673e+003	1.000e+003	1.24008e+002
5.044e+002	1.673e+003	1.000e+003	1.17291e+002
5.346e+002	1.673e+003	1.000e+003	1.11136e+002
5.648e+002	1.673e+003	1.000e+003	1.05506e+002
5.950e+002	1.673e+003	1.000e+003	1.00363e+002

Continued on next page

T $[K]$	ρ $[kg/m^3]$	C_p $[J/kg\ K]$	k $[W/m\ K]$
6.252e+002	1.673e+003	1.000e+003	9.56744e+001
6.554e+002	1.673e+003	1.000e+003	9.14058e+001
6.857e+002	1.673e+003	1.000e+003	8.75253e+001
7.159e+002	1.673e+003	1.000e+003	8.40022e+001
7.461e+002	1.673e+003	1.000e+003	8.08069e+001
7.763e+002	1.673e+003	1.000e+003	7.79114e+001
8.065e+002	1.673e+003	1.000e+003	7.52889e+001
8.367e+002	1.673e+003	1.000e+003	7.29138e+001
8.669e+002	1.673e+003	1.000e+003	7.07620e+001
8.971e+002	1.673e+003	1.000e+003	6.88106e+001
9.273e+002	1.673e+003	1.000e+003	6.70382e+001
9.575e+002	1.673e+003	1.000e+003	6.54244e+001
9.877e+002	1.673e+003	1.000e+003	6.39503e+001
1.018e+003	1.673e+003	1.000e+003	6.25985e+001
1.048e+003	1.673e+003	1.000e+003	6.13526e+001
1.078e+003	1.673e+003	1.000e+003	6.01977e+001
1.109e+003	1.673e+003	1.000e+003	5.91201e+001
1.139e+003	1.673e+003	1.000e+003	5.81076e+001
1.169e+003	1.673e+003	1.000e+003	5.71491e+001
1.199e+003	1.673e+003	1.000e+003	5.62351e+001
1.229e+003	1.673e+003	1.000e+003	5.53570e+001
1.260e+003	1.673e+003	1.000e+003	5.45079e+001
1.290e+003	1.673e+003	1.000e+003	5.36822e+001
1.320e+003	1.673e+003	1.000e+003	5.28753e+001
1.350e+003	1.673e+003	1.000e+003	5.20841e+001
1.380e+003	1.673e+003	1.000e+003	5.13071e+001
1.411e+003	1.673e+003	1.000e+003	5.05436e+001
1.441e+003	1.673e+003	1.000e+003	4.97946e+001
1.471e+003	1.673e+003	1.000e+003	4.90622e+001

Continued on next page

T $[K]$	ρ $[kg/m^3]$	C_p $[J/kg\ K]$	k $[W/m\ K]$
1.501e+003	1.673e+003	1.000e+003	4.83500e+001
1.531e+003	1.673e+003	1.000e+003	4.76628e+001
1.562e+003	1.673e+003	1.000e+003	4.70067e+001
1.592e+003	1.673e+003	1.000e+003	4.63893e+001
1.622e+003	1.673e+003	1.000e+003	4.58192e+001
1.652e+003	1.673e+003	1.000e+003	4.53066e+001
1.682e+003	1.673e+003	1.000e+003	4.48630e+001
1.713e+003	1.673e+003	1.000e+003	4.45010e+001
1.743e+003	1.673e+003	1.000e+003	4.42347e+001
1.773e+003	1.673e+003	1.000e+003	4.40795e+001

Appendix B

Characteristic Based Stabilisation

B.1 Introduction

To follow is an outline of how the characteristic based stabilisation method was constructed in the context of the one-dimensional advection-diffusion equation, as referred to in Section 3.4.1.2.

B.2 Method Outline

Equation (3.19) can be written in the following form:

$$\frac{\partial \phi}{\partial t} = -u_1 \frac{\partial \phi}{\partial x_1} + \alpha \frac{\partial^2 \phi}{\partial x_1^2} \quad \forall \quad x_1 \in \mathcal{V}, \quad t \in \mathcal{I} \tag{B.1}$$

A second degree Taylor-series expansion of the dependent variable ϕ at time step $t + \Delta t$, based on ϕ at time step t, results in the semi-discrete expression:

$$\frac{\phi^{t+\Delta t} - \phi^t}{\Delta t} = \left.\frac{\partial \phi}{\partial t}\right|^t + \frac{1}{2}(\Delta t) \left.\frac{\partial^2 \phi}{\partial t^2}\right|^t + O\left[(\Delta t)^2\right] \tag{B.2}$$

where Δt is the time step increment size. Considering the first term on the right-hand side (RHS) of Equation (B.2):

$$\left.\frac{\partial \phi}{\partial t}\right|^t = (-R_{conv} + R_{diff})|^t \tag{B.3}$$

where

$$R_{conv} = u_1 \frac{\partial \phi}{\partial x_1} \tag{B.4}$$

and

$$R_{diff} = \alpha \frac{\partial^2 \phi}{\partial x_1^2} \tag{B.5}$$

Substituting Equation (B.3) back into Equation (B.2) yields:

$$\frac{\phi^{t+\Delta t} - \phi^t}{\Delta t} \approx (-R_{conv} + R_{diff})|^t + \frac{1}{2}(\Delta t) \left.\frac{\partial^2 \phi}{\partial t^2}\right|^t \tag{B.6}$$

which is seen to represent Equation (B.1) with the addition of an additional term which is denoted $\mathcal{D}$, i.e.

$$\mathcal{D} = \frac{1}{2}(\Delta t) \left.\frac{\partial^2 \phi}{\partial t^2}\right|^t \tag{B.7}$$

Here $\mathcal{D}$ is responsible for stabilization of the finite volume numerical procedure (Zienkiewicz & Taylor [81]). Equation (B.7) is now expanded as:

$$\begin{aligned}
\frac{1}{2}(\Delta t) \left.\frac{\partial^2 \phi}{\partial t^2}\right|^t &= \frac{1}{2}(\Delta t) \left[\frac{\partial}{\partial t}\left(\frac{\partial \phi}{\partial t}\right)\right]\Bigg|^t \\
&= \frac{1}{2}(\Delta t) \left[\frac{\partial}{\partial t}(-R_{conv} + R_{diff})\right]\Bigg|^t \\
&= -\frac{1}{2}(\Delta t) \left.\frac{\partial R_{conv}}{\partial t}\right|^t + \frac{1}{2}(\Delta t) \left.\frac{\partial R_{diff}}{\partial t}\right|^t
\end{aligned} \tag{B.8}$$

which is seen to consist of two components, i.e. a component of convective and the other of diffusive nature.

The diffusive term denoted by R_{diff} in Equation (B.3) is known to be well behaved and oscillation free (as long as Δt restrictions are adhered to). It is

therefore not required to stabilize this term and hence the diffusive component of the stabilization term as given by Equation (B.8) is dropped. Kallinderis [35] omits the diffusive component of the stabilization term on account of it being very expensive to calculate. The author however argues that it may be omitted on numerical grounds, as the R_{diff} spatial term is known to be well behaved.

The convective term is dealt with next. Define a Lagrangian reference frame $\phi = \phi(x_1', t)$ where x_1' moves at the convective information propagation velocity u_1 therefore: $dx_1' = dx_1 - u_1 dt$ where the Eulerian reference frame is chosen such that $dx_1 = 0$. It is now possible to specify no function value change from the Eulerian to Lagrangian reference frames:

$$\frac{D\phi}{Dx_1'} = \frac{\partial \phi}{\partial x_1} \tag{B.9}$$

for x_1' corresponding to x_1 given u_1 and dt, where D/Dx_1' denotes the Lagrangian derivative. The relation between the Eulerian and Lagrangian reference frame as per Batchelor [3], applied to $\partial R_{conv}/\partial t$ gives:

$$\frac{DR_{conv}}{Dt} = \frac{\partial R_{conv}}{\partial t} + (u_1 - u_1') \frac{\partial R_{conv}}{\partial x_1} \tag{B.10}$$

where u_1' is the convective component as it appears in the Lagrangian system. For the purpose of the derivation $u_1' = 0$. Expanding Equation (B.10) gives:

$$\frac{DR_{conv}}{Dt} = \frac{d}{dt}\left(u_1 \frac{\partial \phi}{\partial x_1}\right) + u_1 \frac{d}{dx_1}\left(u_1 \frac{\partial \phi}{\partial x_1}\right) \tag{B.11}$$

Now noting that if:

$$\frac{dx_1'}{dt} = -u_1 \tag{B.12}$$

as $dx_1' = -u_1 dt$ $(dx_1 = 0)$

$$\frac{d}{dt}\left(u_1 \frac{\partial \phi}{\partial x_1}\right) = \frac{dx_1'}{dt}\frac{d}{dx_1}\left(u_1 \frac{\partial \phi}{\partial x_1}\right) \tag{B.13}$$

where Equation B.13 is only zero if $dx_1' = dx_1$. This has important numerical implications. It shows that Δt in front of the stabilizing term is to be chosen such that it corresponds to a convective CFL number of 1 i.e. $\Delta t = \Delta t_{conv} = \Delta x_1 / u_1$. As this is not possible to ensure when $\alpha \neq 0$ on an unstructured stretched mesh,

the well posed nature of the developed equation is nullified. It may however be rectified by replacing Δt in front of the stabilizing term (Equation (B.7)) by $\Delta x_1/u_1$. This ensures spurious-oscillation free solutions at all CFL numbers by ensuring that the Lagrangian derivative to time is zero. In this instance the system being solved is self-adjoint ($dx_1' = dx_1$) (Zienkiewicz & Taylor [81]).

The stabilizing term therefore becomes:

$$\begin{aligned} \mathcal{D} &= -\frac{1}{2}\left(\frac{\Delta x_1}{u_1}\right)\left(-u_1^2\frac{\partial^2\phi}{\partial x_1^2}\right)\Bigg|^t \\ &= \frac{\Delta t_{conv}}{2CFL}u_1^2\,\frac{\partial^2\phi}{\partial x_1^2}\Bigg|^t \end{aligned} \tag{B.14}$$

The final discreet form of the one-dimensional advection-diffusion equation at a non-boundary node, rendered conditionally stable via the introduction of the Lax-Wendroff (CB) method as outlined in the preceding text, is given by:

$$\frac{\phi_m^{t+\Delta t}-\phi_m^t}{\Delta t} = -\frac{1}{\mathcal{V}_m}\sum_{\Upsilon_{mn}\cap\mathcal{V}_m} u_1\overline{\phi}_{mn}^t C_{mn}^1 + \frac{\alpha}{\mathcal{V}_m}\sum_{\Upsilon_{mn}\cap\mathcal{V}_m}\frac{(\phi_n^t-\phi_m^t)}{l_{mn}}t_{mn}^1 C_{mn}^1 + \frac{\Delta t_{conv}}{2CFL\mathcal{V}_m}u_1^2\sum_{\Upsilon_{mn}\cap\mathcal{V}_m}\frac{(\phi_n^t-\phi_m^t)}{l_{mn}}t_{mn}^1 C_{mn}^1 \tag{B.15}$$

Appendix C

Numerical Validation

C.1 Introduction

Evaluation of the predicted results for the SANA benchmark test cases, as detailed in Section 4.3, is continued here by additional comparison with numerical results as published by du Toit *et al.* [15]. The aforementioned published results were generated using the systems CFD simulation code *Flownex*.

C.2 SANA

The two test cases considered are similar to those detailed in Section 4.3, i.e. 5 kW and 35 kW with full-length heating element and helium as working fluid, and the predicted solid-phase temperatures are compared with experimental measurements at three different heights. The results as presented by the author are based on a varying porosity field (Section 4.3).

Specific detail as to the boundary conditions employed in this work is given in Section 2.5. It should be noted that comparison of the predicted temperatures are subject to the boundary conditions employed by the respective parties, which are not clearly known by the author for the case of that used by du Toit *et al.* [15]. Keeping the aforementioned in consideration, the comparative temperatures for

both test cases are seen to be in good agreement. Considering Figures C.1, C.2 and C.3, both the predicted temperature variation through the domain and temperature magnitude are seen to compare favourably for both test cases, with the largest discrepancy near the inner wall at 0.09 m elevation for the 5 kW test case (Figure C.1).

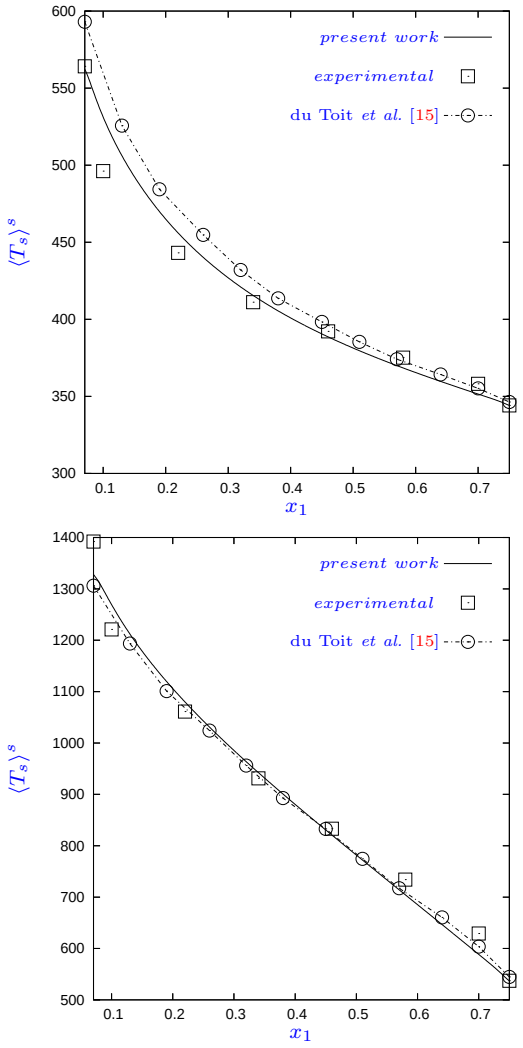

Figure C.1: Predicted pebble temperature distribution at 0.09 m vertical elevation compared to experimental measurements for 5 kW (left) and 35 kW (right).

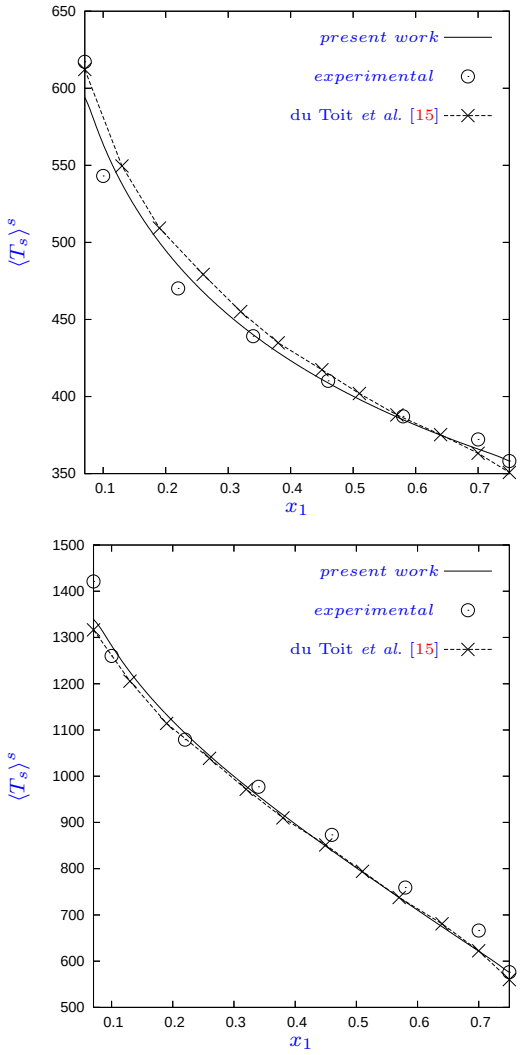

Figure C.2: Predicted pebble temperature distribution at 0.5 m vertical elevation compared to experimental measurements for 5 kW (top) and 35 kW (bottom).

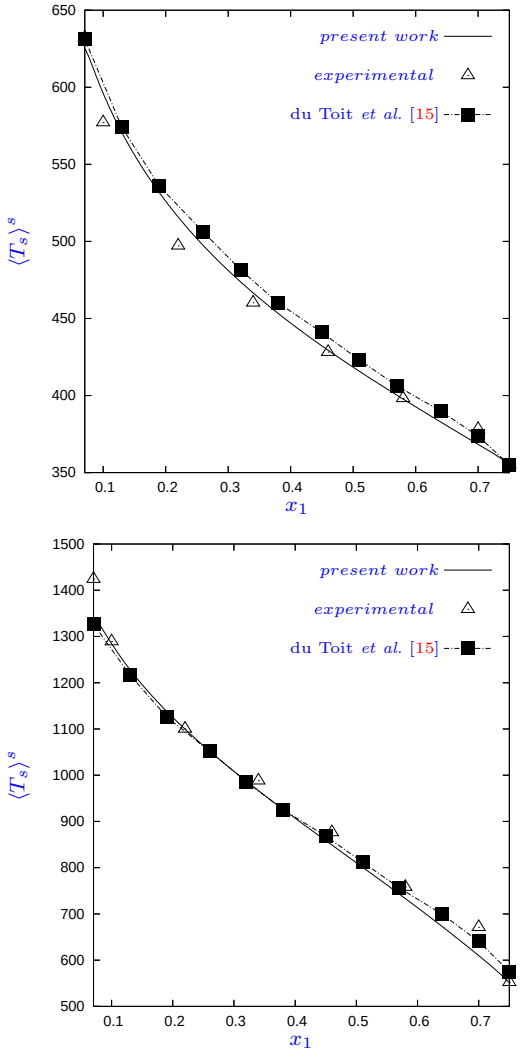

Figure C.3: Predicted pebble temperature distribution at 0.91 m vertical elevation compared to experimental measurements for 5 kW (top) and 35 kW (bottom).

References

[1] Achenbach, E. (1995). Heat and flow characteristics of packed beds. *Experimental Thermal and Fluid Science*, **10**, 17–27. 18

[2] Amiri, A., Vafai, K. & Kuzay, T.M. (1995). Effects of boundary conditions on non-Darcian heat transfer through porous media and experimental comparisons. *Numerical Heat Transfer, Part A*, **27**, 651–664. 25

[3] Batchelor, G.K. (1967). *An Introduction to Fluid Dynamics.*. Cambridge University Press, Cambridge. 67

[4] Bathe, K.J. (1996). *Finite Element Procedures*. Prentice-Hall Inc., London. 38

[5] Bauer, R. & Schlünder, E.U. (1978). Effective radial thermal conductivity of packings in gas flow. Part 2: Thermal conductivity of the packing fraction without gas flow. *International Chemical Engineering*, **18**, 189–204. 21

[6] Becker, S. & Laurien, E. (2003). Three-dimensional numerical simulation of flow and heat transport in high-temperature nuclear reactors. *Nuclear Engineering and Design*, **222**, 189–201. 2, 8, 9, 10, 19

[7] Benenati, R.F. & Brosilow, C.B. (1962). Void fraction distribution in beds of spheres. *A.I.Ch.E. Journal*, **8**, 359–361. vi, 13, 14, 15, 51

[8] Bey, O. & Eigenberger, G. (2001). Gas flow and heat transfer through catalyst filled tubes. *International Journal of Thermal Sciences*, **40**, 152–164. 2

[9] Bonser, D. (2003). Nuclear now for sustainable development. *Nuclear Energy*, **42**, 51–54. 1

[10] Breitbach, G. & Barthels, H. (1980). The radiant heat transfer in the HTR core after failure of the afterheat removal systems. *Nuclear Technology*, **49**, 392–399. 20

[11] Chorin, A.J. (1967). A numerical method for solving incompressible viscous flow problems. *Journal of Computational Physics*, **2**, 12–26. 29

[12] Clery, D. (2005). Nuclear industry dares to dream of a new dawn. *Science*, **309**, 1172–1175. 1

[13] du Toit, C.G. (2002). The pebble-bed reactor: Effect of wall channelling on the flow in the core. In *1st International Conference on Heat Transfer, Fluid Mechanics, and Thermodynamics*, 850–855, Kruger Park, South Africa. 13

[14] du Toit, C.G. (2006). Analysis of the radial variation in the porosity of annular packed beds. In *HTR2006: 3rd International Topical Meeting on High Temperature Reactor Technology*, Johannesburg, South Africa. 14

[15] du Toit, C.G., Rousseau, P.G., Greyvenstein, G.P. & Landman, W.A. (2006). A systems CFD model of a packed bed high temperature gas-cooled nuclear reactor. *International Journal of Thermal Sciences*, **45**, 70–85. 2, 8, 9, 10, 19, 44, 69, 70, 71, 72

[16] Elmo, M. & Cioni, O. (2003). Low mach number model for compressible flows and application to HTR. *Nuclear Engineering and Design*, **222**, 117–124. 12

[17] Ergun, S. (1952). Fluid flow through packed columns. *Chemical Engineering Progress*, **48**, 89–94. 16

[18] Fabis, P.M. & Windischmann, H. (1999). Thermal modeling of diamond-based power electronics packaging. In *Annual* IEEE *Semiconductor Thermal Measurement and Management Symposium*, 98–104. 2

[19] Freiwald, M.G. & Paterson, W.R. (1992). Accuracy of model predictions and reliability of experimental data for heat transfer in packed beds. *Chemical Engineering Science*, **47**, 1545–1560. 19, 26

[20] Fundamenski, W.R. & Gierszewski, P.J. (1991). Comparison of correlations for heat transfer in sphere-pac beds. *Canadian Fusion Fuels Technology Project*, **CFFTP G-9181**, 1–42. 25

[21] Fundamenski, W.R. & Gierszewski, P.J. (1992). Heat transfer correlations for packed beds. *Fusion Technology*, **21**, 2123–2127. 19, 25

[22] Gagarinskii, A.Y., Ignat'ev, V.V., Ponomarev-Stepnoi, N.N., Subbotin, S.A. & Tsibul'skii, V.F. (2005). Role of nuclear power in world energy production in the 21st century. *Atomic Energy*, **99**, 759–769. 1

[23] Gao, Z. & Shi, L. (2002). Thermal hydraulic calculation of the HTR-10 for the initial and equilibrium core. *Nuclear Engineering and Design*, **218**, 51–64. 18

[24] Gidaspow, D. (1986). Hydrodynamics of fluidization and heat transfer: Supercomputer modeling. *ASME Applied Mechanics Reviews*, **39**, 1–23. 8

[25] Giese, M., Rottschäfer, K. & Vortmeyer, D. (1998). Measured and modelled superficial flow profiles in packed beds with liquid flow. *AIChE Journal*, **44**, 484–490. 52

[26] Gnielinski, V. (1981). Equations for the calculation of heat and mass transfer during flow through stationary spherical packings at moderate and high Péclet numbers. *International Chemical Engineering*, **21**, 378–383. 18

[27] Gordon, G. & du Toit, C.G. (2004). Comparison between the experimental and numerical determination of the radial variation in the porosity in cylindrical packed beds. In *Proceedings at the Fourth South African Conference on Applied Mechanics*, Johannesburg. 13

[28] Gotoh, K., Jodrey, W.S. & Tory, E.M. (1978). Variation in the local packing density near the wall of a randomly packed bed of equal spheres. *Powder Technology*, **20**, 257–260. 13

[29] Gunn, D.J. (1978). Transfer of heat or mass to particles in fixed and fluidised beds. *International Journal for Heat and Mass Transfer*, **21**, 467–476. 8, 18

[30] Hoffmann, J.E. (2004). Validation and verification of CFD simulations at PBMR. In *Proceedings at the Fourth South African Conference on Applied Mechanics*, Johannesburg. 2, 19

[31] Hunt, M.L. & Tien, C.L. (1990). Non-darcian flow, heat and mass transfer in catalytic packed-bed reactors. *Chemical Engineering Science*, **45**, 55–63. vi, 13, 14, 15

[32] IAEA (2001). Current status and future development of modular high-temperature gas-cooled reactor technology. Tech. Rep. IAEA-TECDOC-1198, International Atomic Energy Agency. 2

[33] IAEA (2001). Heat transport and afterheat removal for gas-cooled reactors under accident conditions. Tech. Rep. IAEA-TECDOC-1163, International Atomic Energy Agency. 4, 19, 20, 21, 22, 24, 60

[34] Jameson, A., Schmidt, W. & Turkel, E. (1981). Numerical simulation of the Euler equations by finite volume methods using Runge-Kutta timestepping schemes. In *AIAA paper 81-1259, AIAA* 5^{th} *Computational Fluid Dynamics Conference*. 37, 40

[35] Kallinderis, Y. (1996). A 3-D finite-volume method for the Navier-Stokes equations with adaptive hybrid grids. *Applied Numerical Mathematics*, **20**, 387–406. 37, 67

[36] Kaviany, M. (1991). *Principles of Heat Transfer in Porous Media*. Springer-Verlag, New-York. 20

[37] Koster, A., Matzner, H.D. & Nicholsi, D.R. (2003). PBMR design for the future. *Nuclear Engineering and Design*, **222**, 231–245. 2

[38] KTA (1978). Reactor core design of high-temperature gas-cooled reactors. Part 1: Calculation of the material properties of helium. Tech. Rep. KTA3102.1, Nuclear Safety Standards Commission. 24, 60

[39] KTA (1983). Reactor core design of high-temperature gas-cooled reactors. Part 2: Heat transfer in spherical fuel elements. Tech. Rep. KTA3102.2, Nuclear Safety Standards Commission. 18

[40] Kuipers, J.A.M., van Duin, K.J., van Beckum, F.P.H. & van Swaaij, W.P.M. (1992). A numerical model of gas-fluidised beds. *Chemical Engineering Science*, **47**, 1913–1924. 8, 9, 10, 17, 19

[41] Lebon, G. & Cloot, A. (1986). A thermodynamical modelling of fluid flows through porous media: Application to natural convection. *International Journal for Heat and Mass Transfer*, **29**, 381–390. 8

[42] Lecomte, M. (2001). Industrial aspects of revisited HTR's. *Nuclear Engineering and Design*, **209**, 233–241. 2

[43] Lewis, R.W. & Malan, A.G. (2005). Continuum thermodynamic modeling of drying capillary particulate materials via an edge-based algorithm. *Computer Methods in Applied Mechanics and Engineering*, **194**, 2043–2057. 31, 33

[44] Magnico, P. (2003). Hydrodynamic and transport properties of packed beds in small tube-to-sphere diameter ratio: Pore-scale simulation using an Eulerian and a Lagrangian approach. *Chemical Engineering Science*, **58**, 5005–5024. 6

[45] Malan, A.G. (2002). *Investigation into the Continuum Thermodynamic Modelling of Investment Casting Shell-Mould Drying*. Ph.D. thesis, University of Wales, Swansea. 31

[46] Malan, A.G., Lewis, R.W. & Nithiarasu, P. (2002). An improved unsteady, unstructured, artificial compressibility, finite volume scheme for viscous incompressible flows: Part I. Theory and implementation. *International Journal for Numerical Methods in Engineering*, **54**, 695–714. 29, 30, 31, 40

[47] Martin, H. (1978). Low Peclet number particle-to-fluid heat and mass transfer in packed beds. *Chemical Engineering Science*, **33**, 913–919. 13

[48] Massarotti, N., Nithiarasu, P. & Zienkiewicz, O.C. (2001). Natural convection in porous medium - fluid interface problems. The finite element analysis by using the CBS procedure. *International Journal of Numerical Methods for Heat and Fluid Flow*, **11**, 473–490. 37

[49] Mavriplis, D.J. (1990). Accurate multigrid solution of the Euler equations on unstructured and adaptive meshes. *AIAA Journal*, **28**, 213–221. 37, 40

[50] Morris, J.P., Zhu, Y. & Fox, P.J. (1999). Parallel simulations of pore-scale flow through porous media. *Computers and Geotechnics*, **25**, 227–246. 6, 7

[51] Niessen, H.F. & Stöcker, B. (1997). *Data Sets of SANA Experiment: 1994-1996*. JUEL-3409, Forschungszentrum Jülich. vi, vii, 3, 7, 24, 44, 46, 47, 60

[52] Nithiarasu, P., Seetharamu, K.N. & Sundararajan, T. (1999). Numerical investigation of boyancy-driven flow in a fluid-saturated non-darcian porous medium. *International Journal for Heat and Mass Transfer*, **42**, 1205–1215. 7

[53] Pan, C., Hilpert, M. & Miller, C.T. (2001). Pore-scale modelling of saturated permeabilities in random sphere packings. *Physical Review. E, Statistical, Nonlinear, and Soft Matter Physics*, **64**, 066702. 6

[54] PBMR (2007). Website. *http://www.pbmr.com/*. 1

[55] Prasad, V., Kladias, N., Bandyopadhaya, A. & Tian, Q. (1989). Evaluation of correlations for stagnant thermal conductivity of liquid-saturated porous beds of spheres. *International Journal of Heat and Mass Transfer*, **32**, 1793–1796. 21

[56] Prasad, V., Lauriat, G. & Kladias, N. (1992). Non-darcy natural convection in a vertical porous cavity. In *Heat and Mass Transfer in Porous Media.*, 293–314, Elsevier. 8, 13, 51

[57] Price, J. (1968). The distribution of fluid velocities for randomly packed beds of spheres. *Mechanical and Chemical Engineering Transactions*, **1**, 7–14. 52

[58] Radestock, J. & Jeschar, R. (1971). Theoretische untersuchung der gegenseitigen beeinflussung von temperatur- und strömungsfeldern in schüttungen. *Chemie Ingenieur Technik*, **43**, 1304–1310. 16

[59] Roblee, L.H.S., Baird, R.M. & Tierney, J.W. (1958). Radial porosity variations in packed beds. *A.I.Ch.E. Journal*, **4**, 460–464. 13

[60] Robold, K. (1982). Wärmetransport im inneren und in der randzone von kugelschüttungen. Tech. Rep. 1976, Kernforschungsanlage Jülich GmbH. 19

[61] Rowe, M. (2006). Research supports nuclear. *Nuclear Engineering International*, **51**, 30–31. 1

[62] Schmidt, C. (2006). Technology solutions: The next generation of nuclear power. *Environmental Science and Technology*, **40**, 1382–1383. 1

[63] Shuen, J.S., Chen, K.H. & Choi, Y.H. (1993). A coupled implicit method for chemical non-equilibrium flows at all speeds. *Journal of Computational Physics*, **106**, 306–318. 30

[64] Thurgood, C.P., Amphlett, J.C., Mann, R.F. & Peppley, B.A. (2004). Radiative heat transfer in packed beds: the near-wall region. In *Proceedings: AIChE Spring National Meeting*, 257–269, New Orleans. 21, 22

[65] Tsotsas, E. (2002). *Heat Exchanger Design Handbook*. Sec. 2.8.2. 22

[66] Tsotsas, E. & Martin, H. (1987). Thermal conductivity of packed beds: A review. *Chemical Engineering and Processing*, **22**, 19–37. 19

[67] Tsotsas, E. & Schlünder, E.U. (1990). Heat transfer in packed beds with fluid flow: Remarks on the meaning and the calculation of a heat transfer coefficient at the wall. *Chemical Engineering Science*, **45**, 819–837. 26

[68] Vafai, K. (1984). Convective flow and heat transfer in variable porosity media. *Journal of Fluid Mechanics*, **147**, 233–259. 9

[69] Vafai, K., Alkire, R.L. & Tien, C.L. (1985). An experimental investigation of heat transfer in variable porosity media. *ASME Journal of Heat Transfer*, **107**, 642–647. 8, 13, 51

[70] Vahdati, M., Morgan, K., Peraire, J. & Hassan, O. (1989). A cell-vertex upwind unstructured grid solution procedure for high-speed compressible viscous flow. In *Proceedings at the International Conference on Hypersonic Aerodynamics*, 12.1–12.22, Royal Aeronautical Society, London. 31

[71] van Staden, M.P., van Rensburg, C.J. & Viljoen, C.F. (2004). CFD modelling of high-temperature reactors. In *Proceedings at the Fourth South African Conference on Applied Mechanics*, Johannesburg. 8

[72] Verkerk, E.C. (2000). *Dynamics of Pebble-Bed Nuclear Reactor in the Direct Brayton Cycle*. Ph.D. thesis, Delft University of Technology. 2, 3, 8, 18

[73] Vortmeyer, D. & Schuster, J. (1983). Evaluation of steady flow profiles in rectangular and circular packed beds by a variational method. *Chemical Engineering Science*, **38**, 1691–1699. 13

[74] Watson, D.F. (1992). *Contouring, A guide to the Analysis and Display of Spatial Data*. Pergamon Press, New York. 15

[75] Whitaker, S. (1967). Diffusion and dispersion in porous media. *American Institute of Chemical Engineers Journal*, **13**, 420–427. 7

[76] White, S.M. & Tien, C.L. (1987). Analysis of flow channelling near the wall in packed beds. *Wärme- und Stoffübertragung*, **21**, 291–296. 13, 51

[77] Xiong, D., Azar, K. & Tavassoli, B. (2006). High-capacity, compact hybrid air cooling system. In *Thermomechanical Phenomena in Electronic Systems - Proceedings of the Intersociety Conference*, 786–790. 2

[78] Xiong, G., Lu, M., Chen, C.L., Wang, B.P. & Kehl, D. (2001). Numerical optimization of a power electronics cooling assembly. In IEEE *Applied Power Electronics Conference and Exposition* - APEC *2*, 1068–1073. 2

[79] Zehner, P. & Schlünder, E.U. (1970). Wärmeleitfähigkeit von Schüttungen bei mäBigen Temperaturen. *Chemie Ingenieur Technik*, **42**, 933–941. vi, 19, 21, 23

[80] Zienkiewicz, O.C. & Codina, R. (1995). A general algorithm for compressible and incompressible flow. Part I. The split characteristic based scheme. *International Journal for Numerical Methods in Fluids*, **20**, 869–885. 37

[81] Zienkiewicz, O.C. & Taylor, R.L. (2000). *The Finite Element Method: Volume 3 - Fluid Dynamics*. Butterworth-Heinemann, Oxford, 5th edn. 37, 66, 68

[82] Zweben, C. (2006). Thermal materials solve power electronics challenges. *Power Electronics Technology*, **32**, 40–47. 2